

METHODS OF PATTERNING MAGNETIC THIN FILMS WITH  
BLOCK COPOLYMER TEMPLATING

by

ALLEN GLOVER OWEN

SUBHADRA GUPTA, COMMITTEE CHAIR

YANG-KI HONG

DAWEN LI

ROBERT SCHARSTEIN

PATRICK LECLAIR

A DISSERTATION

Submitted in partial fulfillment of the requirement for the degree  
of Doctor of Philosophy in the Department of  
Electrical and Computer Engineering  
in the Graduate School, of  
The University of Alabama

TUSCALOOSA, ALABAMA

2017

Copyright Allen G. Owen 2017  
ALL RIGHTS RESERVED

## ABSTRACT

Increasing the areal density of magnetic hard disk drives has drawn considerable research interest in the last several years. Industry expects that the upper limit of areal density of current granular media storage methods is reached when the grain size becomes small enough to begin losing thermal stability. In this dissertation, we examined methods to fabricate a patterned media that will achieve high areal density without sacrificing thermal stability. We first examined using different block copolymers to template a pattern onto a magnetic thin film. We then tried to improve the patterning and size tuning the nanospheres using different methods of processing the block copolymer. We further examined using the block copolymers to fabricate a hard mask with different materials, and we examined using a powerful method to examine the switching behavior of the patterned magnetic films.

## LIST OF ABBREVIATIONS AND SYMBOLS

SNR	Signal-to-noise Ratio
ML	Multi-Layer
PMA	Perpendicular Magnetic Anisotropy
$H_{\text{eff}}$	Effective Field
$M_s$	Saturation Magnetization
HDD	Hard Disk Drive
$K_u$	Anisotropy Constant
$k_b$	Boltzmann Constant
$\Delta$	Thermal Stability
AGM	Alternating Gradient Magnetometer
RIE	Reactive Ion Etching
AOE	Advanced Oxide Etching
TEM	Tunneling Electron Microscopy
SEM	Scanning Electron Microscopy
RPM	Revolutions Per Minute
SCCM	Standard Cubic Centimeter
$H_{\text{sat}}$	Saturation Field
$H_k$	Anisotropy Field
FWHM	Full Width at Half Maximum

FORC	First Order Reversal Curves
$H_a$	Reversal Field
$H_b$	Incremental Field
$H_c$	Coercivity
FIB	Focused Ion Beam
$\sigma$	Standard Deviation

## ACKNOWLEDGEMENTS

First, I would like to express my deepest thanks to my advisor, Dr. Subhadra Gupta for her support, mentoring and encouragement over the last several years. Without her support, this work would not be possible.

I offer my deepest thanks to my committee members, Dr. Yang-Ki Hong, Dr. Robert Scharstein, Dr. Dawen Li and Dr. Patrick LeClair for their advice, help and mentoring over the years. Their advice and constructive criticism made this work better than I could have made it alone.

I would like to thank Dr. Alton Highsmith, the staff of the CAF, Mr. Rich Martens, Mr. Rob Holler, Mr. Johnny Goodwin, the MINT staff, Dr. Michael Buettner and John Hawkins for their technical expertise and support. Their help was critical to the success of this work.

I would like to thank the Micro Fabrication Facility, the director of MINT, Dr. Takao Suzuki, the Electrical and Computer Engineering department, The Seagate Corporation and the National Science Foundation “GOALI Nanopatterned Graded Media” (0901858) for their financial support over the years.

I would like to thank Dr. Peiter Visscher for his help with FORC analysis. I would like to thank Dr. Anusha Natarajarathinam, Dr. Hao Su, Dr. Amritpal Singh, and future-Dr. Bill Clark for their help, mentoring and friendship. Mr. Robert Douglas is the first of a long list of undergraduates I would like to thank for their help on this project.

Finally, I need to thank my parents for being patient with my unusually long stay in school, and their support and encouragement, and love.

## CONTENTS

ABSTRACT.....	ii
LIST OF ABBREVIATIONS AND SYMBOLS.....	iii
ACKNOWLEDGEMENTS.....	v
LIST OF TABLES.....	x
LIST OF FIGURES.....	xi
1. INTRODUCTION.....	1
1.1 BACKGROUND OF HARD DISK STORAGE AND BIT PATTERNED MEDIA.....	1
1.2 MAGNETIC MATERIALS FOR BIT PATTERNED MEDIA.....	4
1.2.1 PERPENDICULAR VS LONGITUDINAL MAGNETIC MEDIA.....	4
1.2.2 SWITCHING FIELD DISTRIBUTION AND FIRST ORDER REVERSAL CURVES.....	5
1.3 FABRICATION METHODS FOR BPM.....	6
1.3.1 E-BEAM LITHOGRAPHY.....	6
1.3.2 DIRECTED SELF ASSEMBLY OF BLOCK COPOLYMERS.....	6
1.3.3 NANOIMPRINT LITHOGRAPHY.....	8
1.4 DISSERTATION OUTLINE.....	8
2. EQUIPMENT.....	10
2.2 FABRICATION.....	10
2.2.1 SPUTTERING.....	10

2.2.2 ION MILLING.....	13
2.2.3 PLASMA TREATMENT.....	14
2.2.4 E-BEAM EVAPORATION.....	15
2.3. MAGNETIC CHARACTERIZATION.....	15
2.3.1 ALTERNATING GRADIENT MAGNETOMETER (AGM).....	15
2.4 STRUCTURAL CHARACTERIZATION OF THIN FILMS.....	17
2.4.1 X-RAY DIFFRACTION/REFLECTIVITY.....	17
2.4.2 SCANNING ELECTRON MICROSCOPE.....	18
3. HEPTANE SOLVENT ANNEALING VS. THERMAL ANNEALING.....	19
3.1 INTRODUCTION.....	19
3.2 EXPERIMENTAL DETAILS.....	20
3.3 RESULTS AND DISCUSSION.....	21
3.4 CONCLUSIONS.....	29
4. BIT PATTERNING MEDIA USING P2VP-PDMS BLOCK COPLOYMER AND CR HARD MASK.....	30
4.1 INTRODUCTION.....	30
4.2 EXPERIMENTAL DETAILS.....	30
4.3 RESULTS AND DISCUSSION.....	32
4.3.1 P2VP-B-PDMS ETCH MASK.....	32
4.3.2 100 NM CR HARD MASK.....	44
4.3.3 30 NM CR HARD MASK.....	47
4.3.4 20 NM CR HARD MASK.....	49
4.4 CONCLUSIONS.....	52

5. NANOPATTERNING MAGNETIC MEDIA USING ULTRASONIC SIZE TUNED BLOCK COPOLYMERS.....	53
5.1 INTRODUCTION.....	53
5.2 EXPERIMENTAL DETAILS.....	53
5.3 RESULTS AND DISCUSSION.....	54
5.4 CONCLUSIONS.....	58
6. FIRST ORDER REVERSAL CURVES STUDY OF PATTERNED MEDIA.....	59
6.1 INTRODUCTION.....	59
6.2 EXAMPLE FROM HEPTANE ANNEALING STUDY.....	63
6.3 EXAMPLE FROM COPD ALLOY PATTERNING.....	65
6.4 CONCLUSIONS.....	67
7. OVERALL CONCLUSIONS.....	69
REFERENCES.....	72

## LIST OF TABLES

Table 7.1 Magnetic Thin Films Investigated.....	71
---	----

## LIST OF FIGURES

Figure 1.1 ASTC technology roadmap compass.....	2
Figure 1.2 Comparison of conventional media and bit patterned media.....	3
Figure 1.3 P2VP-b-PDMS with (a),(b) lamella, (c),(d) hexagonally perforated lamella, (e),(f) cylinder, (g),(h) sphere morphologies.....	7
Figure 2.1 (a) Photo of system and (b)schematic of SFI Shamrock system in UA-MFF.....	11
Figure 2.2 Schematic of S-gun cathode in SFI Shamrock system.....	12
Figure 2.3 Isotropic vs. Anisotropic etching.....	13
Figure 2.4 Intelvac ion mill system .....	14
Figure 2.5 Photo of SPTS AOE and schematic of ICP chamber of SPTS AOE tool.....	15
Figure 2.6 (a) Princeton Scientific AGM and (b) schematic.....	16
Figure 2.7 (a) Phillips x-ray diffractometer and (b) schematic.....	17
Figure 2.8 (a) Photo of JEOL 7000F SEM and (b) schematic.....	18
Figure 3.1 Out-of-plane M-H loop of unpatterned Ta 5/Pd 5/[Co0.3/Pd1.0]14/Ta 3 nm film...22	22
Figure 3.2 SEM images showing (a) air-annealed sample pre-etch (b) heptane-annealed sample pre-etch (c) air-annealed sample after etching at 45° and 4 min (d) heptane-annealed sample after etching 45° and 3.5 min.....	23
Figure 3.3 Plot of (a) coercivity and (b) squareness versus etch time and etch angles of 30°, 45°, 55°, and 80° for air-annealed samples.....	24
Figure 3.4 Out-of-plane M-H loops for air annealed samples etched at (a) 30° (b) 45° (c) 55° (d) 80° for 2, 2.5, 3, 3.5, and 4 minutes.....	25
Figure 3.5 Plot of (a) coercivity and (b) squareness vs etch time and etch angles of 30°, 45°, 55°, 80° for heptane annealed samples.....	26
Figure 3.6 Out of plane M-H loops for heptane annealed samples ion milled at (a) 30°;(b) 45°;(c) 55°;(d) 80° for 2,2.5 3, 3.5, and 4 minutes.....	27

Figure 3.7 Contour plot of coercivity vs etch angle and etch time for air annealed matrix.....	28
Figure 3.8 Contour plot of coercivity vs etch angle and etch time for heptane annealed matrix.....	29
Figure 4.1 Cr Hard Mask Process.....	32
Figure 4.2 Full film out of plane M-H loop of Pd <sub>5</sub> [Co <sub>0.3</sub> Pd <sub>1.0</sub> ] <sub>8</sub> Pd 5 nm thin film.....	33
Figure 4.3 Out of plane M-H loops for samples etched at 60° for 5-30 sec at 200 V beam voltage.....	34
Figure 4.4 Out of plane M-H loops for samples etched at 70° for 5-30 sec at 200 V beam voltage.....	35
Figure 4.5 Out of plane M-H loops for samples etched at 80° for 5-30 sec at 200 V beam voltage.....	35
Figure 4.6 Out of plane M-H loops for samples etched at 60° for 1-4 sec at 100 V beam voltage.....	36
Figure 4.7 Out of plane M-H loops for samples etched at 70° for 1-4 sec at 100 V beam voltage.....	37
Figure 4.8 Out of plane M-H loops for samples etched at 80° for 1-4 sec at 100 V beam voltage.....	38
Figure 4.9 SEM micrographs showing samples (a) As deposited and after etching at (b) 60° for 1 sec (c) 60° 1 sec.....	39
Figure 4.10 Etch Time vs coercivity for etch angles of 60°-80° etched at 200 V.....	39
Figure 4.11 Etch time vs. coercivity for etch angle of 60° etched at 100 V.....	40
Figure 4.12 Etch time vs. coercivity for etch angle of 70°.....	41
Figure 4.13 Etch time vs. coercivity for etch angle of 80°.....	42
Figure 4.14 Contour plot of coercivity vs. etch angle and time.....	43
Figure 4.15 SFD vs Etch time.....	44
Figure 4.16 M-H loop of sample etched at 60° for 2 sec.....	45
Figure 4.17 M-H loop after etching 1 min at 70°.....	46

Figure 4.18 Series of M-H loops after etching at 70° for (a) 15 sec (b) 30 sec (c) 45 sec (d) 60 sec (e) 5 min and (f) 10 min.....	47
Figure 4.19 Coercivity, squareness, SFD vs etch time for samples with 100 nm etched at 70°.....	47
Figure 4.20 SEM micrographs of 1000 Å Cr after etching at 70° for (a) 1min (b) 5 min.....	48
Figure 4.21 M-H loops of Pd5[Co0.3Pd1.0]Pd 5 nm magnetic stack with P2VP-PDMS and 30 nm Cr coat ion milled at 70° for (a) 45 sec, (b) 60 sec, (c) 75 sec and ion milled at 80° for (d) 45 sec, (e) 60 sec and (f) 75 sec.....	49
Figure 4.22 Coercivity, squareness and SFD for samples with 30 nm Cr, etched at 70°.....	49
Figure 4.23 Coercivity, squareness and SFD for samples with 30 nm Cr, etched at 80°.....	49
Figure 4.24 M-H loops of Pd5[Co0.3Pd1.0]Pd 5 nm magnetic stack with P2VP-PDMS and 20 nm .....	51
Figure 4.25 Coercivity, squareness and SFD for samples with 20 nm Cr, etched at 60°.....	52
Figure 4.26 Coercivity, squareness and SFD for samples with 20 nm Cr, etched at 70°.....	52
Figure 4.27 Coercivity, squareness and SFD for samples with 20 nm Cr, etched at 80°.....	53
Figure 5.1 Full film out-of-plane M-H loop of Ta5/Pd5/Co <sub>25</sub> Pd <sub>75</sub> 20/Ta5 nm stack.....	55
Figure 5.2 SEM micrograph of PS-b-PFS nanospheres after (a)2 hr ultrasonic in toluene bath (b) etch 55° 1:45 min.....	56
Figure 5.3 Out-of-plane M-H loops of samples etch at 55° for (a) 30 sec (b) 45 sec (c) 1 min (d) 1:15 min.....	57
Figure 5.4 Out-of-plane M-H loops of samples etch at 55° for (a) 1:30 min (b) 1: 45 min (c) 2 min (d) 2:45 min.....	58
Figure 5.5 Coercivity, squareness and SFD vs. etch time.....	58
Figure 6.1 Idealized FORC example (a) FORC distribution (b) positive bias M-H loop (c) negative bias M-H loop .....	62
Figure 6.2 (a) Point selection and interpolation (b) FORC calculation. ....	63
Figure 6.3 (a) FORC curves and (b) VARIFORC distribution of heptane annealed sample etched at 45° 3.5 min .....	64

Figure 6.4 (a) FORC curves and (b) FORC+ distribution of heptane annealed sample etched at 45° 3.5 min .....65

Figure 6.5 FORC curves and (b) VARIFORC distribution of CoPd alloy sample etched at 55° 1:45 min.....66

Figure 6.6 FORC curves and (b) FORC+ distribution of CoPd alloy sample etched at 55° 1:45 min.....67

## 1. INTRODUCTION

### 1.1. BACKGROUND OF HARD DISK STORAGE AND BIT PATTERNED MEDIA

With the introduction of the hard disk drive in 1956, the disk drive industry has been able to make great strides in increasing the storage capacity of disk drives from 5 megabytes for the first storage unit by IBM to multiple terabytes in 2014, representing an annual increase of over 30% for the last sixty years<sup>1</sup>. Annual increases in areal density in recent years has slowed to less than 15% due to difficulties in further improving the capabilities of conventional recording media<sup>1</sup>, which consists of a continuous thin film of CoCrPt granular magnetic material<sup>1</sup>. It has been assumed for the last several years that the maximum achievable areal density of granular media would be reached when reducing the grain size would result in loss of thermal stability of the media<sup>1</sup>. Industry has set a goal of achieving 10 Tb/in<sup>2</sup> by 2025, as seen in Figure 1.1 below.

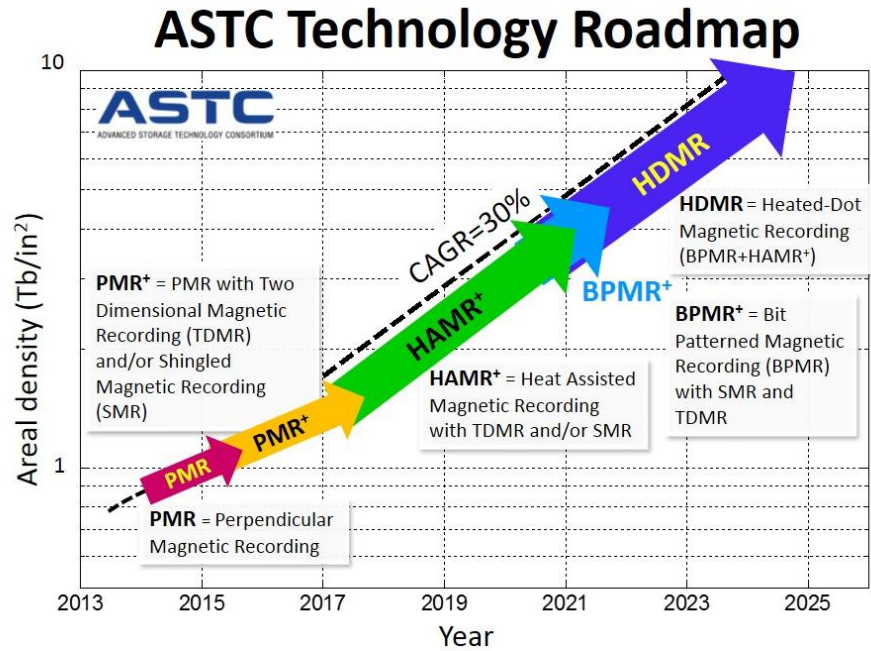


Figure 1.1 ASTC Technology roadmap (<http://www.idema.org/?page%20id=5868>)

Thermal stability, signal-to-noise ratio (SNR) and media writability are described as the “trilemma” of magnetic recording media; mutually exclusive objectives in magnetic storage media design<sup>2</sup>. It has become obvious that before this “trilemma” has been reached that scaling granular media to support areal densities of greater than 1 Tb/in<sup>2</sup> is already challenging<sup>1</sup>. There have been a number of technologies proposed that might show moderate increases in areal density, two of which address the fundamental problems of conventional media. Heat assisted magnetic recording<sup>3</sup> and microwave assisted magnetic recording<sup>4</sup> both allow further reduction in size of granular media by increasing the write field and using higher coercivity media with good thermal stability. Heat assisted magnetic recording heats the magnetic material above the material’s Curie temperature, making it easier to change the magnetization. Microwave assisted magnetic recording uses a radio frequency field to switch the magnetization of the material. However, both technologies suffer from the same shortcoming typical of granular media, such as low SNR.

The other option is bit patterned magnetic recording media, which replaces granular media with lithographically patterned islands of magnetic materials. These patterned islands are somewhat larger than the random grains of conventional media, resulting in both high SNR and thermal stability<sup>5-7</sup>. The theoretical aspects of bit patterned magnetic recording physics have been thoroughly explored in the literature<sup>8-11</sup>. An island of single layer magnetic material switches in a way that is well described by Stoner-Wohlfarth theory<sup>12</sup> and is simple. Exchange coupled composite media, where multiple materials are combined to create writable, thermally stable islands to achieve the desired areal density also possesses simple recording physics<sup>13, 14</sup>. Neither of these methods suffer from the complications from noise and grain size distributions of granular media. A comparison between conventional media and bit patterned media is shown in Figure 1.2 below. The difficulty for bit patterned media design lies in fabrication, where limitations in lithography, imprinting, and etch methods are constraints.

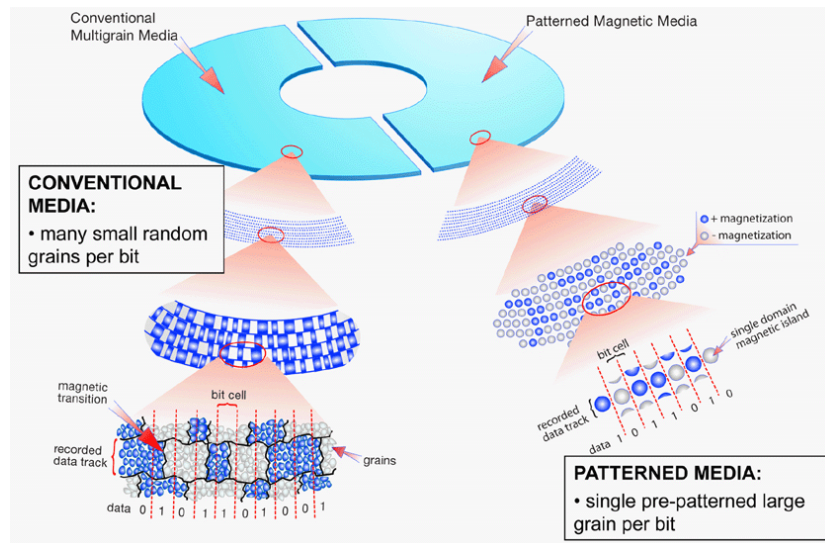


Figure 1.2 Comparison of conventional media and bit patterned media

An important consideration for bit patterned media is thermal stability. The thermal stability,  $\Delta$  is given by

$$\Delta = \frac{KV}{k_B T} \quad (1.1)$$

where  $K$  is the anisotropy energy,  $V$  is the volume,  $T$  is temperature and  $k_B$  is Boltzmann's constant. If the magnetic islands are too small, their magnetism can flip randomly with thermal fluctuations. The thermal stability is a function of volume and magnetic anisotropy. The Néel-Arrhenius<sup>15</sup> equation can be used to estimate the reversal rate and it is given by

$$\tau_N = \tau_0 \exp(KV/k_B T) \quad (1.2)$$

where  $\tau_N$  is the average switching time due to thermal fluctuations, and  $\tau_0$  is the attempt time characteristic of the material. If  $\Delta$  is maintained at an average of  $\sim 40$ , then the media will be thermally stable for 10 years. Dipole fields can contribute to thermal instability as well as residual write fields.

## 1.2. MAGNETIC MATERIALS FOR BIT PATTERNED MEDIA

### 1.2.1 PERPENDICULAR VS LONGITUDINAL MAGNETIC MEDIA

The switch to perpendicular magnetic anisotropy media from longitudinal magnetic anisotropy media was important because as the recording density of the longitudinal medium increases, the effective fringing field demagnetizes the neighboring bit, while for perpendicular magnetic media, the effective field stabilizes the neighboring bits against demagnetization<sup>16</sup>. The effective field for longitudinal magnetic anisotropy materials is given<sup>17</sup> by

$$H_{eff} = H_{K\parallel} + 2\pi M_s \quad (1.3)$$

For perpendicular magnetic anisotropy media, the out-of-plane anisotropy is given by

$$H_{K\perp} > 4\pi M_s \quad (1.4)$$

and the effective field is

$$H_{eff} = H_{K\perp} - 4\pi M_s \quad (1.5)$$

where  $H_k$  is the anisotropy field,  $H_{eff}$  is the effective field, and  $M_s$  is the saturation magnetization. Equation 1.2 and 1.4 are derived by adding the demagnetization tensor multiplied by the saturation magnetization. For an applied field in the x- and y-direction (in-plane) the demagnetization tensor is -1/2 as for the shape anisotropy of a cylinder, while for an applied field in the z-direction (perpendicular), the demagnetization tensor is 1 as for a flat plate. Examining equations 1.3 and 1.5, we can see that the longitudinal media has to overcome a demagnetization field that is not present in perpendicular media.

### 1.2.2 SWITCHING FIELD DISTRIBUTION AND FIRST ORDER REVERSAL CURVES

In principle, the initial films for bit-patterned media must be continuous, smooth and uniform so that they can be patterned into uniform magnetic islands. In practice, significant differences in physical structure and properties can occur among the array of islands. These differences can cause variations in the switching field of the islands, often referred to as the switching field distribution (SFD)<sup>18-21</sup>. The switching field distribution has several components, such as thermal effects, defects, grain boundaries, crystal orientation, seed layer effects, edge damage, edge oxidation<sup>22-30</sup> as well as broadening from dipolar fields from neighboring islands<sup>31</sup>. The SFD needs to be kept as narrow as possible to ensure the write head properly reverses the island without disturbing the magnetic state of the island's neighbors. The SFD is determined by

calculating and plotting  $dM/dH$  and fitting a Gaussian distribution to the  $dM/dH$  plot. The full width at half maximum of the Gaussian distribution is then divided by the coercivity of the M-H loop to yield the SFD, which is often reported as a percentage in literature<sup>18-21</sup>.

First Order Reversal Curve distributions are a more sophisticated way of looking at magnetization reversal<sup>32-36</sup>. This will be discussed in detail in Chapter 6.

## 1.3 FABRICATION METHODS FOR BPM

### 1.3.1 E-BEAM LITHOGRAPHY

In electron beam (e-beam) lithography, a focused electron beam is scanned on a surface coated with an electron sensitive polymer called a resist. The electron beam alters the solubility of the resist, allowing selective removal of either the exposed or non-exposed resist by immersing the surface in a solvent. The primary advantage of e-beam lithography is the ability to pattern with a resolution of  $<10$  nm. However, e-beam lithography is not suitable for high volume manufacturing due to low throughput, since it is a direct-write technique.

### 1.3.2 DIRECTED SELF ASSEMBLY OF BLOCK COPOLYMERS

Di-block copolymers consist of two immiscible polymeric blocks connected by a covalent bond. They phase separate to a minimum interaction volume, which is driven by segregation strength, given by  $\chi N$ , where  $\chi$  is the Flory-Huggins interaction parameter and  $N$  is the degree of polymerization<sup>37</sup>. To use a block copolymer to fabricate BPM, a block copolymer thin film is used instead of resist and one of the blocks is removed to leave the other block as a mask for pattern transfer, very similar to resist masks used in traditional lithography. Depending upon the block copolymer and the phase separation method used, morphologies that block copolymers can form are spheres, cylinders and lamellae or hexagonally perforated lamellae<sup>38</sup>. As an example, poly(2-

vinylpyridine-b-dimethylsiloxane) (P2VP-b-PDMS) can form different morphologies depending on the solvent used for phase separation, as seen in Figure 1.3 below.

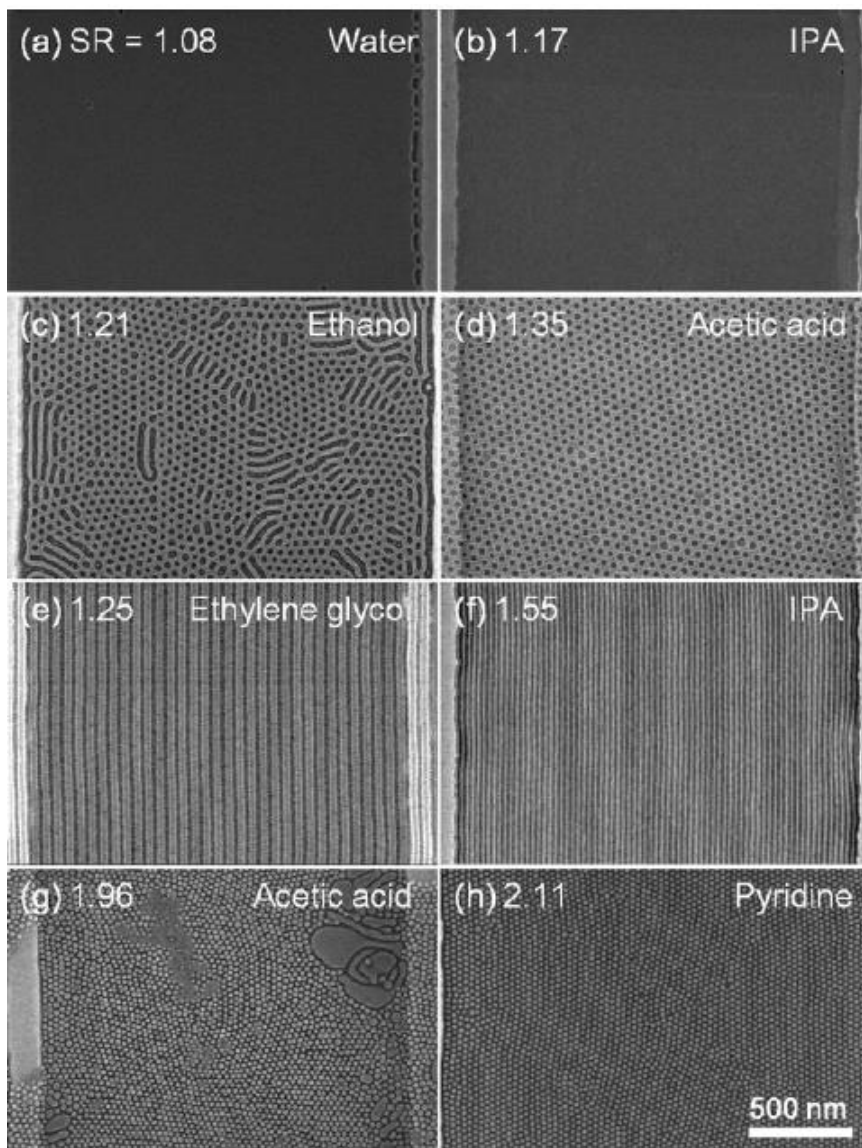


Fig. 1.3 P2VP-b-PDMS with (a),(b) lamella, (c),(d) hexagonally perforated lamella, (e),(f) cylinder, (g),(h) sphere morphologies<sup>39</sup>.

### 1.3.3 NANOIMPRINT LITHOGRAPHY

For low cost, high throughput fabrication of BPM, nanoimprint lithography<sup>40-42</sup> is the preferred technique and was developed specifically for the fabrication of BPM<sup>43</sup>. Nanoimprint lithography is a method of transferring a pattern onto a substrate using a fabricated template. An imprint resist is dispensed onto the surface of the substrate, after which the template and substrate are placed into contact, and after a curing process, the template and substrate are separated. Although nanoimprint lithography can produce high throughput BPM, defects arising from poor adhesion, template release and mechanical contacts occur<sup>1</sup>. Templates are produced using e-beam lithography, have a limited lifetime, and can be damaged by particles on the surface of the imprinted substrate<sup>1</sup>.

### 1.4 DISSERTATION OUTLINE

Chapter 2 presents the experimental procedures involved in optimizing bit patterned media using block copolymer lithography techniques. Sputter deposition using the SFI Shamrock system is explained. Etching using an Intelvac ion mill system is detailed. Characterization of the as deposited and etched films using alternating gradient magnetometer (AGM) is explained. X-ray diffraction (XRD) to examine the structure of the films is detailed. Scanning electron microscopy (SEM) to study the morphology of the films is described.

Chapter 3 compares different phase separation methods for block copolymer lithography. The effects of solvent annealing with heptane are discussed and compared with thermal annealing in atmosphere. Magnetic measurements and surface morphology of the two-phase separation methods are discussed. Chapter 4 presents an examination of patterning media using P2VP-b-PDMS block copolymer. Magnetometry and surface morphology of the fabricated nanopillars are

presented and discussed. The effect of using a Cr hard mask in conjunction with the P2VP-b-PDMS block copolymer is discussed. Chapter 5 discusses using ultrasound and a solvent bath to size tune PFS nanospheres to fabricate smaller nanostructures. Chapter 6 discusses first order reversal curves to study the switching mechanisms of patterned films. Chapter 7 presents our conclusions.

## 2. EQUIPMENT

### 2.1 INTRODUCTION

The main purpose of this project was to optimize the best method for nano-patterning perpendicular magnetic anisotropy material. The thin film multilayers were deposited in the UA Micro-Fabrication Facility (MFF) using a SFI Shamrock 7-gun planetary sputtering system. Characterization of the crystal structure and morphology of the thin film multilayers was carried out by X-ray diffraction (XRD) on a Phillips X'Pert X-ray diffractometer and scanning electron microscopy (SEM) using a JEOL 7000F FEG-SEM located in the Central Analytical Facility (CAF) and the Center for Materials for Information Technology (MINT).

Magnetic characterization was carried out on a Princeton Scientific MicroMag 2900 alternating gradient magnetometer in MINT. Nanopatterned magnetic arrays were fabricated using a SPTS advanced oxide etcher (SPTS-AOE) and an Intelvac ion mill with a Veeco ion source in UA-MFF. Vacuum annealing was carried out in using the lamp array in the Shamrock as well as in a custom-built furnace annealer in MINT. This chapter will discuss the equipment used in the growth, fabrication and analysis of the patterned thin films.

### 2.2 FABRICATION

#### 2.2.1 SPUTTERING

Sputtering is the ejection of atoms from a material by bombardment of the material by positive ions. Sputtering is used by industry to manufacture magnetic storage for personal computers, optical coatings and in semiconductor fabrication. The UA Micro-Fabrication Facility

(uamicro) possesses a SFI Shamrock sputter deposition tool [Figure 2.1 (a)] which has a base pressure of  $2 \times 10^{-8}$  Torr and was used to deposit all the films discussed here.

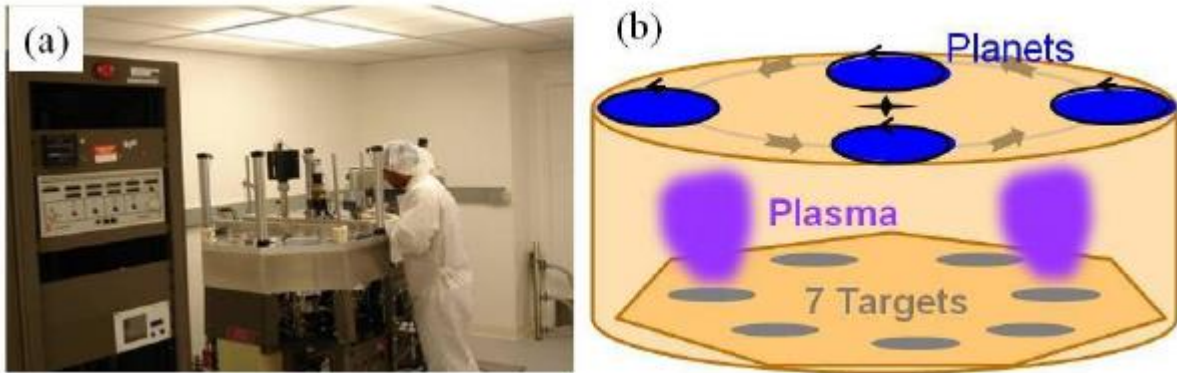


Figure 2.1 (a) Photo of system and (b) schematic of SFI Shamrock system in UA-MFF [Ref. 44]

Sputter deposition of all materials was carried out with the SFI Shamrock sputter deposition system. It is a fully automated planetary deposition system with seven 3” diameter cathode positions designed for physical vapor deposition (PVD) of magnetic, non-magnetic and insulating materials. One of the cathode positions is used for infrared lamps for rapid thermal annealing before or after deposition. The SFI Shamrock can operate in one of two operating modes; the “InTouch™” mode or in the man-machine interface mode (MMI). The MMI software directly interfaces with the software that runs the Mystic programmable logic controllers, which allows direct interfacing with the hardware. The “InTouch™” software mode is used for one-button operation and is recipe driven, controlling the entire process sequence, from loading the wafers to deposition. This allows batches of four substrates to be processed using the “InTouch™” control mode.

The S-gun magnetron consists of an anode, a cathode and a magnetic field to contain the electrons. Permanent magnets are arrayed around the cathode in such a way the magnetic flux is

parallel to the target surface and intercepts two corners of the target, confining the ions and electrons to the surface of the target. The area of heaviest target erosion is called the “racetrack”, and the ions and electrons move around the “racetrack” with a drift velocity proportional to the cross-product of the electric and magnetic fields. The cathodes are powered by AC, DC or RF supplies. Reactive sputtering of oxides and nitrides is made possible by sputtering with a partial pressure of the appropriate reactive gases. Sputtering parameters for depositions in this project were Ar+ ion pressure of 2 mTorr and powers ranged from 50-300 W.

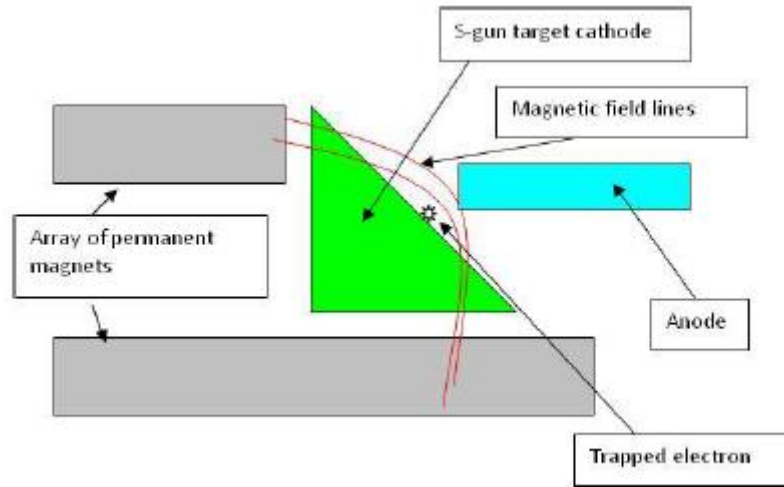


Figure 2.2 Schematic of S-gun cathode in SFI Shamrock system [Ref. 44]

The system consists of a sputter module (SM), and transfer module (TM) and a cassette module (CM). The cassette module is a loadlock to load and unload wafers, with a cassette holder that can hold up to 16 6” diameter AlTiC substrates. We used 3” diameter Si wafers or smaller pieces affixed to the AlTiC substrates for our experiments. The transfer module is used to transfer the wafer from the cassette module to the sputter module. Before the wafer is transferred to the sputter module, the turntable must be aligned. Once the alignment is complete, a robotic arm

retrieves the wafer from the cassette module to the sputter module by rotating the arm through 180 degrees. The turntable can turn at speeds of 11, 22, and 44 rpm. The sputter module is pumped down via a turbomolecular pump and a water pump. It also has bake-out heaters. An overnight pump down with the heaters on allows the sputter module to reach base pressures of  $9 \times 10^{-9}$  Torr.

### 2.2.2 ION MILLING

Ion milling is a plasma based etching method where anisotropic etching of the substrate can pattern the wafer resulting in no hazardous waste. Ion milling can be thought of as atomic sand blasting, but instead of sand, argon ions are accelerated with high energy to bombard the wafer surface in a vacuum chamber to remove material. The wafer is mounted on a rotating chuck to ensure uniform removal of material. Since the mask is also under  $\text{Ar}^+$  bombardment, the mask needs to last longer than the target materials to ensure pattern transfer. Ion milling has the advantage of being highly directional, anisotropic and therefore reduces undercuts, i.e. isotropic etching.

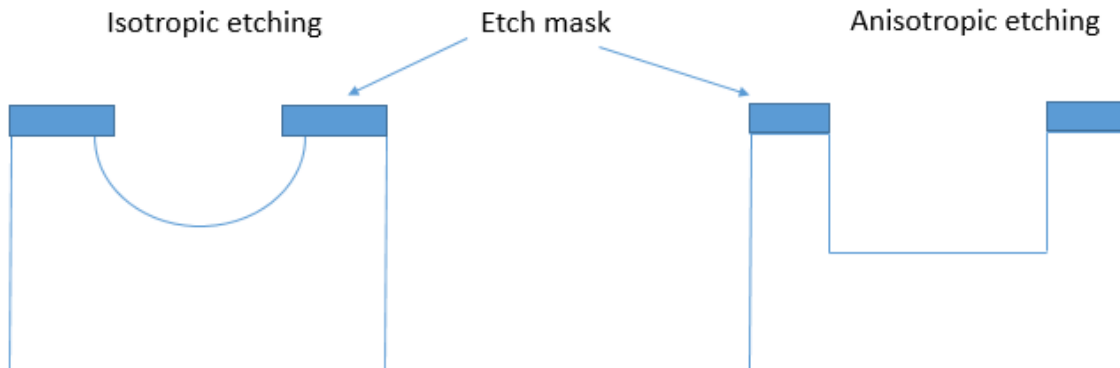


Fig. 2.3 Isotropic vs. Anisotropic etching



Figure 2.4 Intelvac ion mill system [Ref. 45]

### 2.2.3 PLASMA TREATMENT

The SPTS advanced oxide etcher (SPTS-AOE) is a load locked, high frequency inductively coupled plasma (ICP) etch system. The system is configured for dielectric etching and O<sub>2</sub> cleaning, operating at 13.56 MHz. Independent energy control is done by biasing the platen via automatic power control and impedance matching. De-ionized water is used to cool the platen, while helium cools the backside of the substrate. The gases used for etching are O<sub>2</sub>, CF<sub>4</sub>, C<sub>4</sub>F<sub>8</sub>, H<sub>2</sub>, He and Ar. It can load no more than two 4" substrates manually. It can etch dielectric materials such as glass, quartz, other oxides and various polymers very rapidly. It can also etch metals at a relatively low rate. The high-density plasma ( $\sim 10^{12}$  ions cm<sup>-2</sup>) results in a high etch rate at low bias and a low-pressure process leads to good anisotropy and independent ion energy. We used it to remove the polystyrene from the block copolymer PS-PFS with oxygen plasma, and to remove the oxide underneath the hard Cr mask described in Chapter 4.

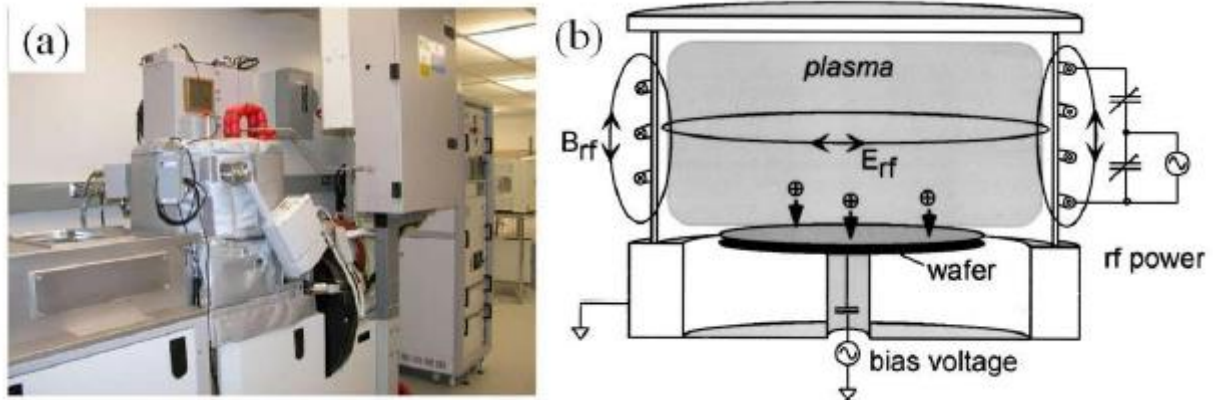


Figure 2.5 Photo of SPTS AOE and schematic of ICP chamber of SPTS AOE tool. [Ref 45]

## 2.2.4 E-BEAM EVAPORATION

The Denton E-beam Evaporation deposition tool uses an electron beam to evaporate a material onto a substrate that is rotating above the heated material. The chamber is pumped down to a pressure  $\sim 1 \times 10^{-6}$  Torr. The electron beam is accelerated to a high kinetic energy and is directed onto the evaporation material by a magnetic field. The kinetic energy of the electrons is converted into thermal energy, heating the evaporation material. When the temperature and pressure is at a certain point, the material will melt or sublime, resulting in a vapor that coats the substrate. The accelerating voltage and current is typically 6-8 kV and a 10-15 mA. This tool was used to deposit Cr and  $\text{SiO}_2$  onto wafers with magnetic thin films.

## 2.3. MAGNETIC CHARACTERIZATION

### 2.3.1 ALTERNATING GRADIENT MAGNETOMETER (AGM)

An alternating gradient magnetometer was used to measure the magnetic moment and the coercivity of the as deposited and patterned films. The sample is mounted at the tip of a glass rod, which in turn is attached to a piezoelectric element. The force from the alternating gradient field

exerted on the sample produces a bending moment on the piezoelectric element, which generates a voltage proportional to the force on the sample and operates at the resonant frequency of the gradient field. The AGM software automatically determines the mechanical resonance and the operating frequency of the sample. The amplitude of the voltage from the piezoelectric element is proportional to the magnetic moment of the sample and the hysteresis loop can be obtained by changing the applied DC field<sup>46</sup>. Before measurements are made, the system must be calibrated with magnetic material of a known magnetic moment. In this case, the system was calibrated with a yttrium garnet with a magnetic moment of 82.02 memu/cc. The system was used to measure both M-H loops and FORC curves.

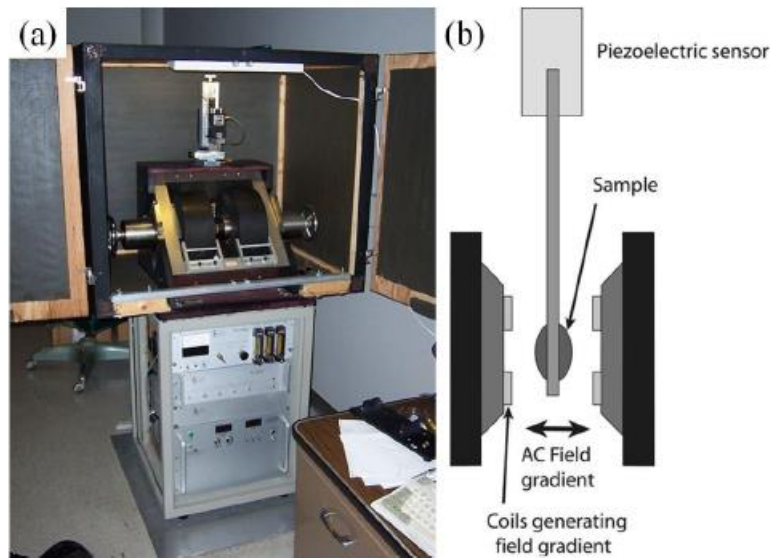


Figure 2.6 (a) Princeton Scientific AGM and (b) schematic [Ref. 45].

## 2.4 STRUCTURAL CHARACTERIZATION OF THIN FILMS

### 2.4.1 X-RAY DIFFRACTION/REFLECTIVITY

X-ray diffraction measurements were carried out to characterize the crystal structure and X-ray reflectivity measurements were done to determine the thickness of the deposited films. Solid matter is either amorphous or crystalline. The crystal unit cell has dimensional axes  $a$ ,  $b$ , and  $c$ , with corresponding angles  $\alpha$ ,  $\beta$ , and  $\gamma$ . When an X-ray beam strikes an atom, the electrons around the atom begin to oscillate at the same frequency as the X-ray beam striking it. This causes destructive interference in all directions. Therefore, there is no energy leaving a solid sample if it is amorphous. In a crystalline material, there will be a few instances of constructive interference, where the X-ray beams will be in phase and will leave the material in various directions. The diffraction pattern is based on Bragg's Law and Cu-K $\alpha$  radiation was used to verify the deposition rate of sputter targets.

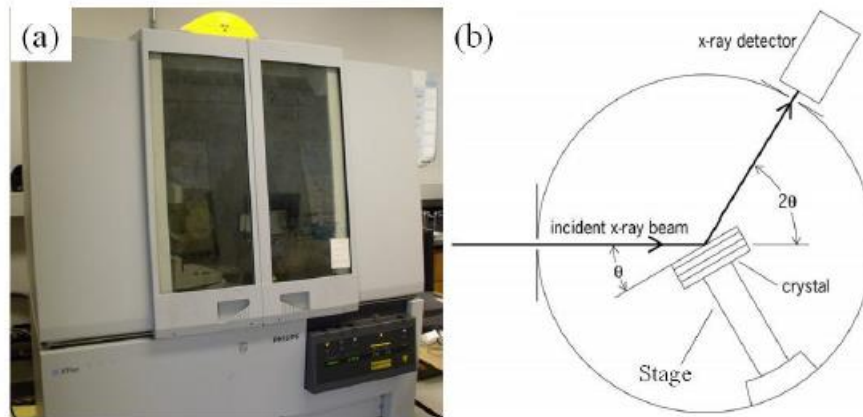


Figure 2.7 (a) Phillips x-ray diffractometer and (b) schematic [Ref. 45]



### 3. HEPTANE SOLVENT ANNEAL VS. THERMAL ANNEALING

#### 3.1 INTRODUCTION

As the areal density of perpendicular magnetic recording (PMR) keeps increasing, a problem known as the ‘trilemma of PMR’ remains to be resolved. This refers to the difficulty of satisfying the conflicting requirements of high signal-noise-ratio (SNR), thermal stability and writability.<sup>8,48-</sup>  
<sup>49</sup> In order to increase density, the media grain size has to be reduced, but it will cause SNR to decrease and becomes thermally unstable due to volume shrinkage. If high magnetic anisotropy materials such as FePt is used, the required write field is too high to be reached by current heads, which causes the writability issue. To solve this problem, bit patterned media (BPM) and heat assisted magnetic recording (HAMR) have been proposed and intensively researched.<sup>48-59</sup> A single island of magnetic material represents one bit in BPM. The islands are naturally exchange decoupled because of the space between them.<sup>48,53</sup> Using Co/Pd multilayers patterned by block copolymers (BCP) researchers have demonstrated an areal density of ~ 1 Tb/in.<sup>48,52,53</sup> In a typical block copolymer lithographic process,<sup>48,55,57</sup> a magnetic film is first deposited and then spin-coated with a block copolymer. Due to its intrinsic properties, blocks of BCP self-assemble and form nanostructured spheres, and selective removal of the surrounding matrix makes these isolated nanospheres form etch masks during the ion milling process. Among various methods to facilitate phase separation,<sup>60-66</sup> solvent annealing, which exposes the block copolymer to a solvent during the annealing, has demonstrated that it can increase the block chain mobility and affect the

interaction between blocks. It may thus change the effective periodic length of block copolymer.<sup>64-</sup>

66

In this chapter, a systematic study comparing BCP phase separation techniques for nanopatterning perpendicular magnetic anisotropy (PMA) Co/Pd multilayers was carried out to determine which method produced a higher packing density as well as higher coercivity. The polystyrene (PS) was phase separated from the polyferrocenyldimethylsilane (PFS) in a PS-PFS block copolymer after spin coating onto a Si substrate. The phase separation was carried out by thermal annealing at atmosphere and by solvent annealing, using heptane to drive off the solvent (toluene) in which the BCP was dissolved. Nanopillars that demonstrated significantly increased coercivity have been successfully fabricated.

### 3.2 EXPERIMENTAL DETAILS

Two designs of experiments (DoE) were undertaken to compare and contrast two methods of phase separation annealing of polystyrene-*b*-polyferrocenyldimethylsilane (PS-*b*-PFS) block copolymer etch mask for bit patterned media<sup>57,60,61</sup>. Each DoE used four etch angles and four etch times in the ion mill, for a total of 16 samples per DoE<sup>67</sup>. Film stacks of Ta 5/Pd 5/[Co 0.3/Pd 1.0]<sub>14</sub>/Ta3 nm were sputter deposited onto Si substrates using a SFI Shamrock planetary sputtering system. The bottom layers of Ta5/Pd5 served as a seed layer for the multilayered Co/Pd stack, while the Ta on top served as a capping layer. The base pressure before deposition was  $5 \times 10^{-8}$  Torr and the Ar sputtering pressure was maintained at 2 mTorr with DC magnetron sputtering powers ranging from 50-250 W.<sup>12,21</sup>

A 1.5 wt % solution of PS-*b*-PFS BCP with a molecular weight of  $68,000 \text{ g mol}^{-1}$  (PS:  $M_w = 55,000 \text{ g mol}^{-1}$ , PFS:  $M_w = 13,000 \text{ g mol}^{-1}$ ,  $M_w/M_n = 1.2$ ) was produced by dissolving the block

copolymer in toluene. The block copolymer was spin-coated onto two Si substrates with identical stacks of magnetic material using a Solitec spin-coater set to 4000 RPM for 40 sec. In order to phase separate the PS from the PFS, one wafer was placed in a Blue M oven set at 140 °C and allowed to anneal in air for 48 hours. The other wafer was solvent annealed by placing the wafer sample in a sealed jar with heptane, which was placed in an oil bath heated to 35° C for 6 hours.

65,66

In order to expose the PFS nanospheres as an etch mask, the PS matrix was ashed away using oxygen plasma in a SPTS Deep Reactive Ion Etch (DRIE) system. The plasma was maintained for 4 minutes at a coil power of 350 W, with an oxygen pressure of 17 mTorr. The patterns were transferred to the magnetic films by argon ion milling in an Intelvac system with an 8 cm Veeco ion source. The beam power was set to 13 W. The angle of the ion beam to the substrate was varied from 30° to 80° and the etch times were varied from 2 min to 4 min in 0.5 min increments. The patterned samples were imaged by scanning electron microscopy (SEM) with a JEOL 7000 FE-SEM. The magnetic properties were measured at room temperature by a PMC Micromag 2900 alternating gradient force magnetometer (AGM) with a maximum applied field of 18 kOe.

### 3.3 RESULTS AND DISCUSSION

Figure 3.1 shows the out-of-plane M-H loops of the as-deposited Ta<sub>5</sub>/Pd<sub>5</sub>/[Co<sub>0.3</sub>/Pd<sub>1.0</sub>]<sub>14</sub>/Ta 3 nm thin film. The Co/Pd film is clearly perpendicular, as shown in Figure 3.1. The squareness  $S^*$ , which is defined as the ratio of remnant magnetization,  $M_r$ , to saturation magnetization,  $M_s$ , is 0.9 and the coercivity is 1.3 kOe.

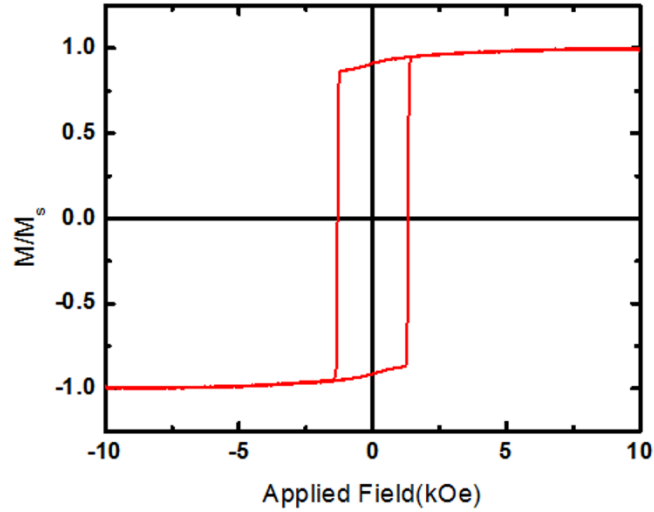


Fig. 3.1 Out-of-plane M-H loop of unpatterned Ta 5/Pd 5/[Co0.3/Pd1.0]14/Ta 3 nm film.

In order to pattern the thin film, we employed a block copolymer templating method, using PS-b-PFS.<sup>14,15</sup> After removing the PS matrix, Figures 3.2(a) and 3.2(b) show a monolayer of PFS nanospheres after air annealing and heptane annealing, respectively. Figure 3.2(c) shows nanopillars fabricated after ion milling at 45° and 4 min for air annealing, and Figure 3.2(d) shows nanopillars fabricated after ion milling at 45° and 3.5 min for heptane solvent annealing. It should be noted that the light square in Figure 3.2(d) was due to electron damage when imaging the picture in the SEM. The average diameter of the nanospheres of the air-annealed samples after the PS was removed by plasma ashing was found to be  $18.6 \pm 2.2$  nm, while the average diameter of the nanospheres of the heptane-annealed samples was found to be  $25.3 \pm 2.5$  nm. It appears that the heptane annealing caused the PFS to phase separate to a greater degree than air annealing, yielding larger nanospheres.<sup>64, 66</sup> The average diameter of the nanopillars of the air-annealed samples after etching was found to be  $22.7 \pm 2.1$  nm, while the average diameter of the nanopillars of the heptane-annealed samples was found to be  $33.6 \pm 3.2$  nm. The cause of the size increase after etching can be attributed to the self-shadowing effect of the PFS nanospheres during the ion milling process.<sup>60</sup>

<sup>68</sup> It was observed that etching for a long period of time at near normal incidence ( $80^\circ$ ) smoothed the surface which is possibly caused by the disappearance of the PFS mask under these etching conditions.<sup>60</sup>

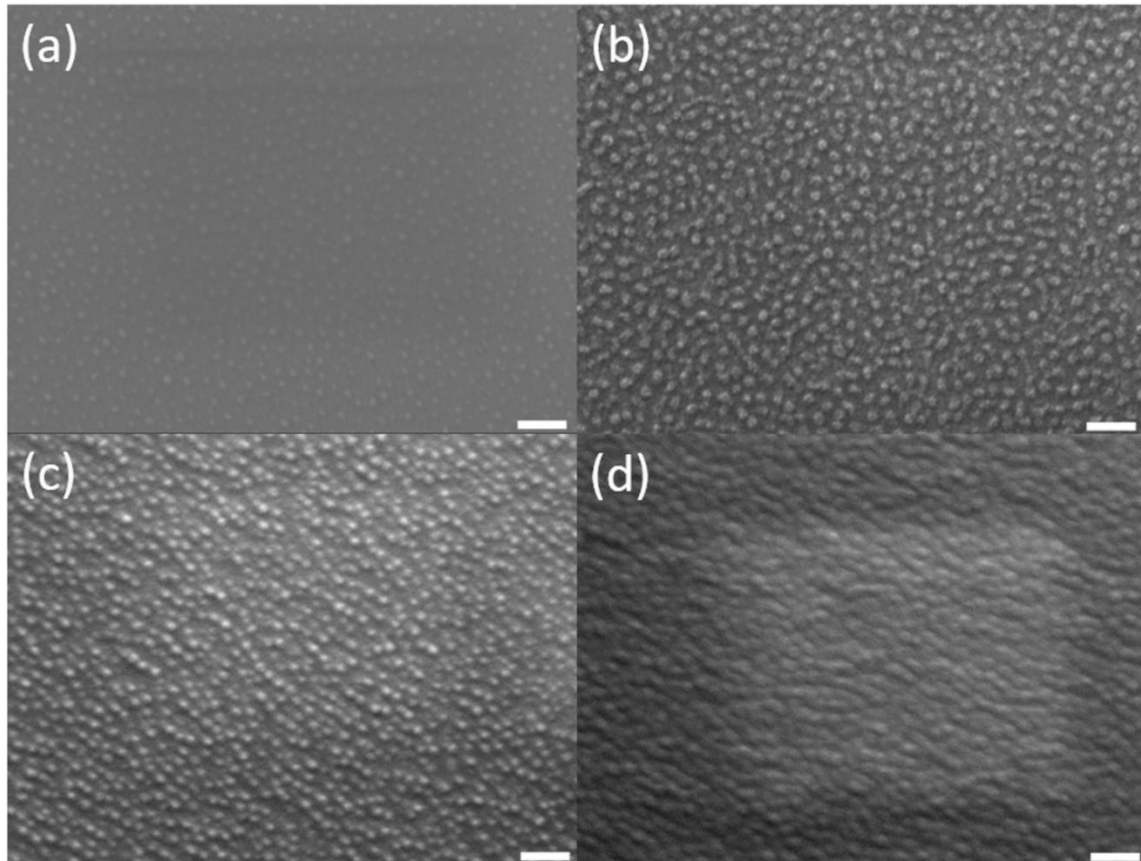


Fig. 3.2 SEM images showing (a) air-annealed sample pre-etch (b) heptane-annealed sample pre-etch (c) air-annealed sample after etching at  $45^\circ$  and 4 min (d) heptane-annealed sample after etching  $45^\circ$  and 3.5 min. All scale bars are 100 nm.

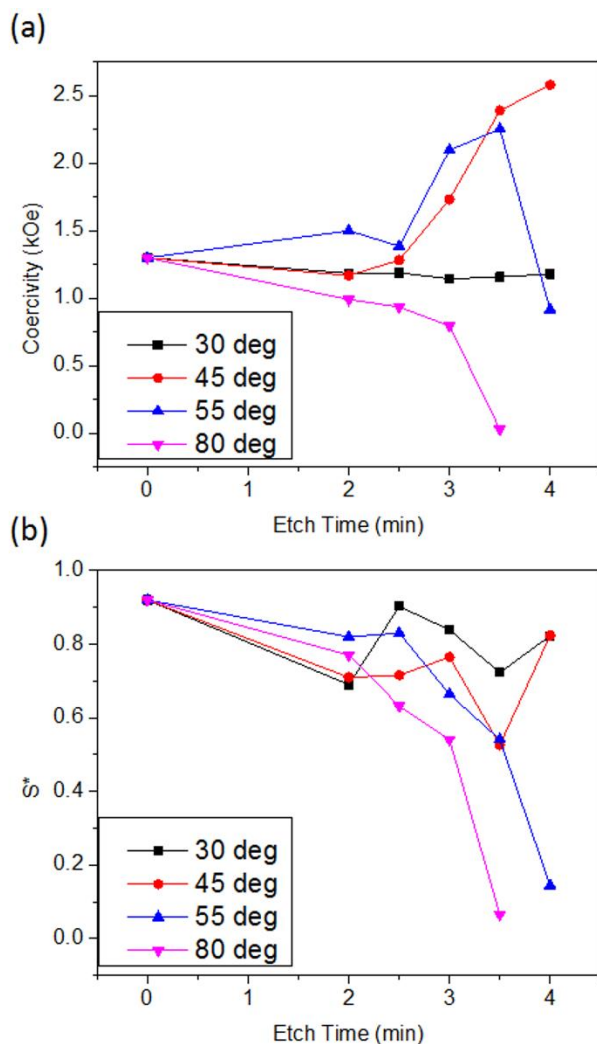


Fig. 3.3 Plot of (a) coercivity and (b) squareness versus etch time and etch angles of 30°, 45°, 55°, and 80° for air-annealed samples.

For the air-annealed series seen in Figure 3 below, the  $S^*$  and coercivity exhibited a decreasing trend with increasing etch time and etch angle in general, except for the etch angles of 30° and 45°. A possible reason for the coercivity remaining more or less constant for the 30° etch angle could be that such a shallow etch angle does not take advantage of the self-shadowing of the nanospheres. Less magnetic material was removed, which means well defined nanopillars were not formed. Enough magnetic material was removed to show a general decreasing trend in  $S^*$ , however. At an angle of 45°, the air-annealed samples exhibited an increase in coercivity, while

there was a concurrent decrease in  $S^*$ , the decreasing trend being slightly more pronounced than for the  $30^\circ$  etch angle. At this angle, the nanospheres can act as an etch mask, using the self-shadowing effect to form nanopillars. At an etch angle of  $55^\circ$ , the air annealed samples exhibited an increase in coercivity, followed by a sharp decrease, while the  $S^*$  steadily decreased. At this etch angle, the etch rate increases and the material is etched away much faster, resulting in less magnetic material. An etch angle of  $80^\circ$  resulted in most of the material being etched away very quickly, resulting in a sharp decrease in coercivity and squareness. Figure 3.4 shows the M-H loops of the air-annealed samples for comparison. It may be noted that, after etching at  $55^\circ$  for 4 minutes, the magnetic material was heavily damaged, and thus yielded abnormal M-H loops.

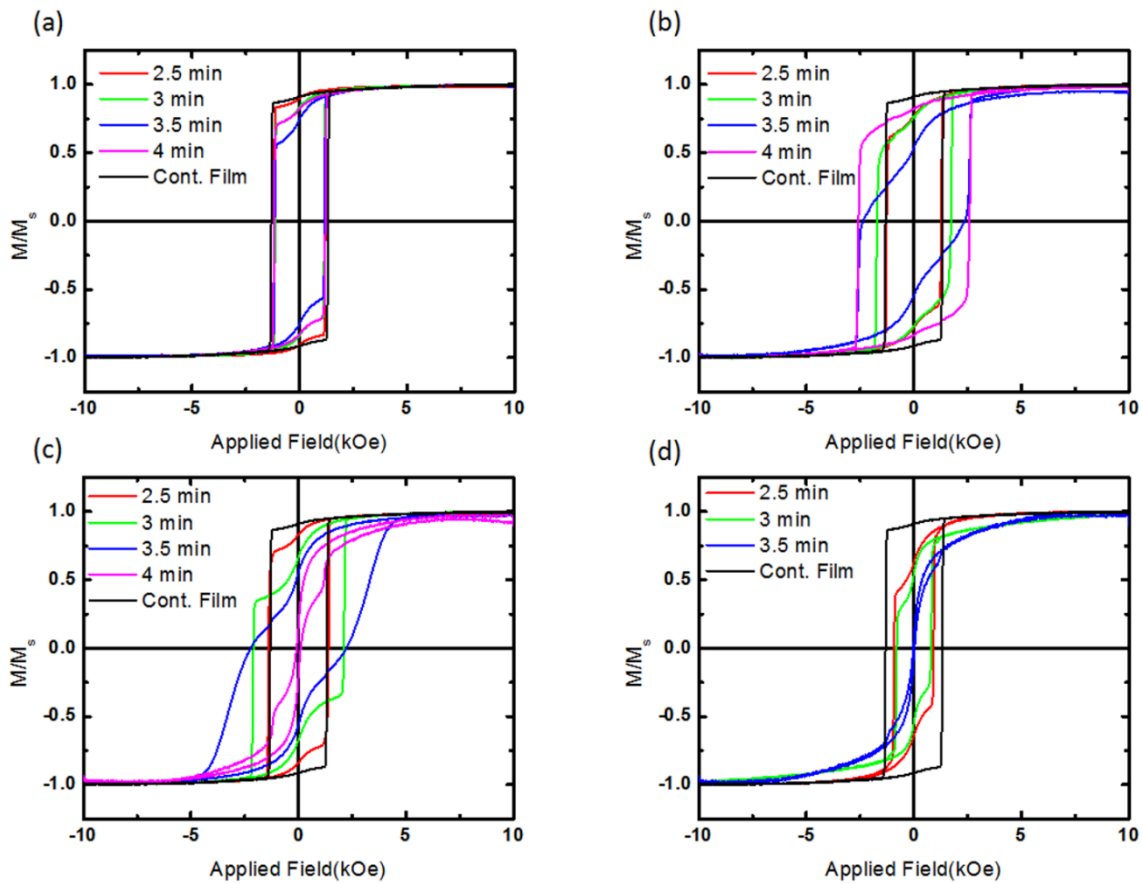


Fig. 3.4 Out-of-plane M-H loops for air annealed samples etched at (a)  $30^\circ$  (b)  $45^\circ$  (c)  $55^\circ$  (d)  $80^\circ$  for 2, 2.5, 3, 3.5, and 4 minutes.

The heptane-annealed samples also exhibited similar trends to the air-annealed samples (see Figure 3.5), including behavior at an etch angle of 45°. The etch angle of 30° resulted in an increase in coercivity until the etch time exceeded 4 minutes, where the coercivity then decreased. As with the air-annealed samples, the heptane-annealed samples etched at 45° showed an increase in coercivity with a concurrent decrease in  $S^*$ , indicating the nanopillars were being formed from self-shadowing. At an etch angle of 55°, the coercivity increased, then decreased sharply, and never equaled or exceeded the coercivity of the 45° etch angle. The squareness decreased steadily.

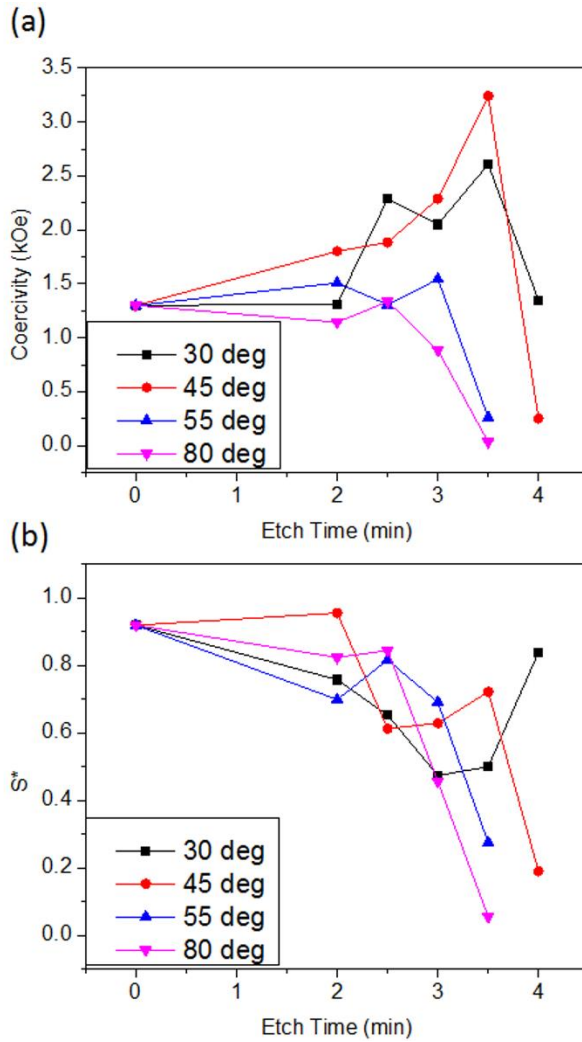


Fig. 3.5 Plot of (a) coercivity and (b) squareness vs etch time and etch angles of 30°, 45°, 55°, 80° for heptane annealed samples.

At an 80° etch angle, the etch rate was much too fast to control well, and both coercivity and squareness decreased. For both the 55° and 80° etch angles, etch times at 4 minutes or greater resulted in magnetic material being etched away such that M-H loops for those data points were not measurable. Figure 3.6 shows all the M-H loops plotted together for comparison.

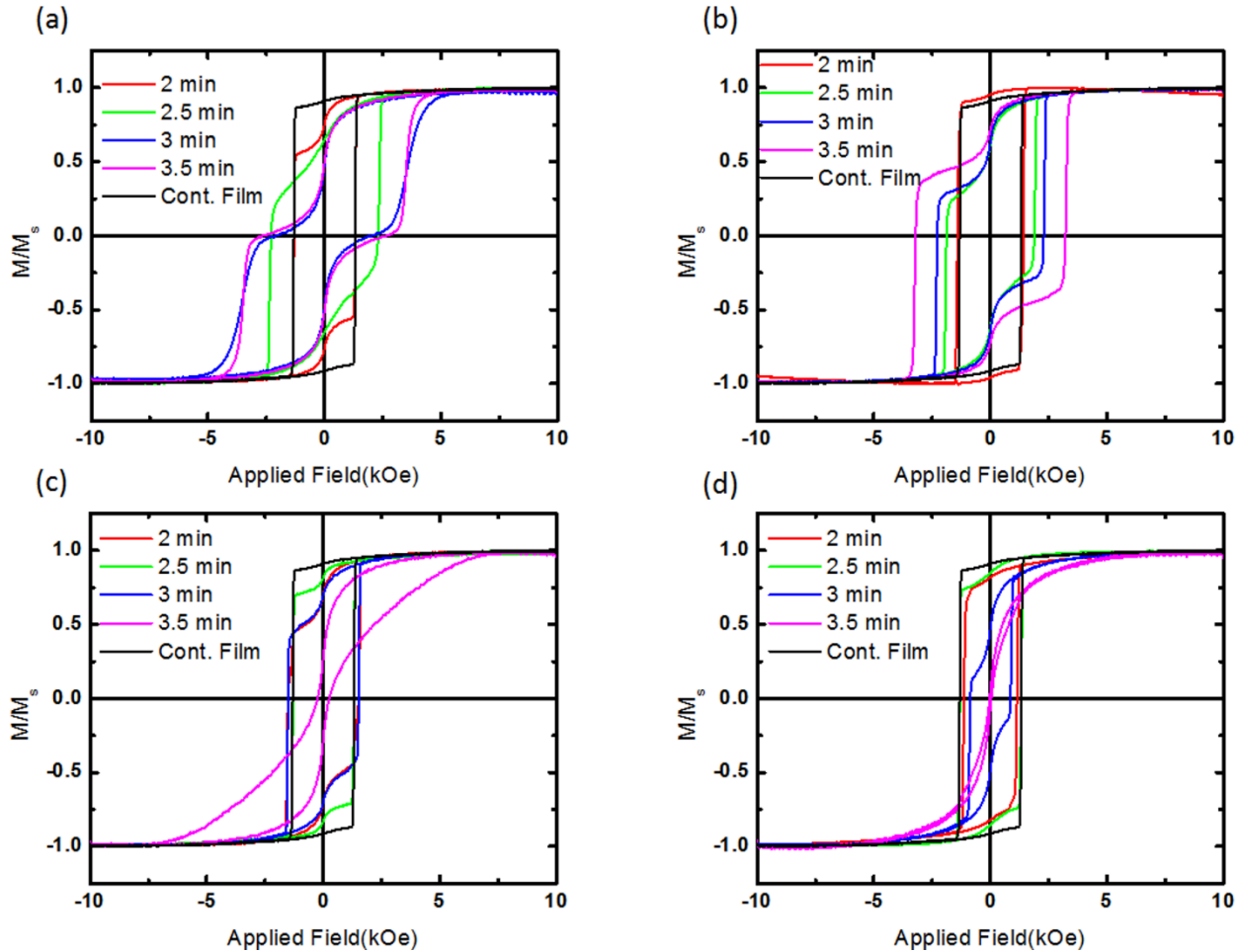


Fig. 3.6 Out of plane M-H loops for heptane annealed samples ion milled at (a) 30°;(b) 45°;(c) 55°;(d) 80° for 2,2.5 3, 3.5, and 4 minutes.

For both air- and heptane-annealed DoEs, the maximum coercivity was achieved at an etch angle of 45° and etch times of 4 and 3.5 minutes, respectively, shown in Figures 3.4(b) and 3.6(b). The M-H loops for the heptane-annealed samples etched at 45° and 3.5 minutes show two

switching fields for this sample, one at a very low field and the other at a coercive field of 3.5 kOe. This implies that there are two regions formed by ion milling that switch at different fields, perhaps consisting of different ratios of Co/Pd. Ion milling damage may also contribute to the different switching fields, since coercivity can be changed by ion irradiation.<sup>69,70</sup> This might also contribute to the two-step switching M-H loops shown in Figure 3.6 (a) for samples etched for 3 and 3.5 minutes.

Contour plots of the two DoEs are shown in Figs 3.7 and 3.8, indicating etching conditions that, statistically, should produce maximum coercivity. For the air-annealed DoE, the contour plot indicates that etch times of 3.25 to 4 minutes with etch angles around 40° to 55° should produce maximum coercivity. However, the range of etch times and etch angles for the heptane-annealed samples are more restrictive, with etch angles from about 40° to 45° and an etch time at 3.5 minutes yielding maximum coercivity. Etching for longer than 4 minutes will result in a decrease in coercivity<sup>59</sup>.

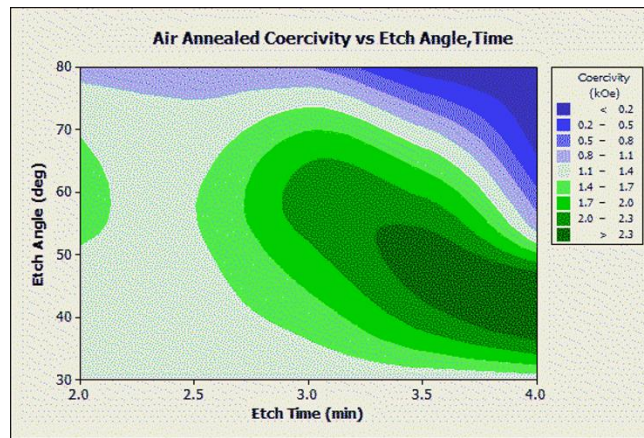


Fig. 3.7 Contour plot of coercivity vs etch angle and etch time for air annealed matrix.

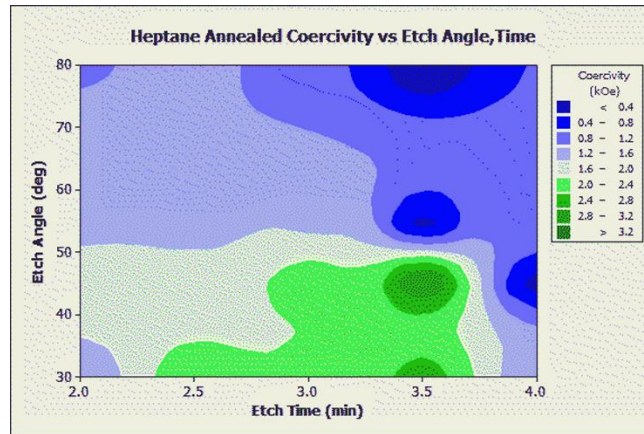


Fig. 3.8 Contour plot of coercivity vs etch angle and etch time for heptane annealed matrix.

### 3.4 CONCLUSIONS

In summary, Co/Pd multilayered nanopillars were patterned by block copolymer templating and two methods of phase separation were compared. A matrix study of etch time and etch angle was undertaken for each phase separation method. It was found that ion milling at  $45^\circ$  and 3.5 minutes for the heptane annealing method yielded the highest coercivity of 3.5 kOe, a 246% increase over the as-deposited coercivity of 1.3 kOe. Future work will involve air annealing the samples first, then heptane annealing to achieve improved phase separation of the PFS spheres.

## 4. BIT PATTERNING MEDIA USING P2VP-PDMS BLOCK COPOLYMER AND CR HARD MASK

### 4.1 INTRODUCTION

After working with PS-b-PFS block copolymer in Chapter 3, we explored a new BCP. A systematic study using poly (2 vinyl-pyridine-b-dimethylsiloxane) (P2VP-b-PDMS) BCP to nanopattern<sup>68</sup> PMA Co/Pd multilayers<sup>71,72,52</sup> was carried out. P2VP-b-PDMS produces smaller nanospheres after phase separation, and should result in greater areal density. In addition, the P2VP-PDMS BCP combined with a Cr hard mask was explored as another patterning technique.

### 4.2 EXPERIMENTAL DETAILS

Pd 5/ [Co 0.3/Pd 1.0]<sub>8</sub>/Pd 5 nm-coated wafers were utilized in this experiment. Each wafer was spin-coated at 4000 rpm for 40 sec on a Solitec spinner with a 1.5 wt % of 13.2 mg of Poly (2-vinyl pyridine-b-dimethylsiloxane) (P2VP-PDMS) block copolymer dissolved in 1 mL of toluene<sup>39</sup>. In order to phase separate the block copolymer, a sample of the coated wafer was solvent annealed in a sealed container with pyridine vapor at room temperature for 24 hours<sup>39</sup>. After the solvent annealing was complete, the coated and annealed sample was plasma ashed with a two step ashing process using the SPTS Advanced Oxide Etcher (AOE) described in Chapter 2. The ashing process first begins with CF<sub>4</sub> plasma with a coil power of 350 W and a bias power of 5 W for 45 sec, followed by O<sub>2</sub> plasma with a coil power of 350 W and a platen power of 0 W for 30 sec<sup>39</sup>.

The first plasma ashing process is to remove the surface layer of PDMS that covers a matrix of P2VP containing PDMS nanospheres. The second plasma ashing process is to remove the P2VP matrix, exposing and oxidizing the PDMS nanospheres. Several matrices of three etch angles and three etch times were completed using argon ion milling with beam voltages of 100-200 V<sup>57,60</sup>. The nanopillars were characterized by magnetometry and SEM.

The patterning process utilizing the Cr hard mask combined with the P2VP-b-PDMS BCP was started in the same way. A 1.5 wt% solution with toluene of P2VP-PDMS block copolymer was spun coated onto the Co/Pd coated wafer and allowed to solvent anneal with pyridine at room temperature for 24 hrs. The block copolymer forms a layer of PDMS on top of a matrix of P2VP embedded with PDMS nanospheres. In order to use the nanospheres as a mask, the PDMS top layer and the P2VP matrix must be removed. This is accomplished by using a two-step plasma ashing step in the AOE. The PDMS top layer is removed with a 50 sec plasma ashing step using CF<sub>4</sub> plasma, and then the P2VP matrix is removed using a 25 sec O<sub>2</sub> plasma process, exposing the PDMS nanospheres.

Co/Pd thin film coated wafers had 20 nm, 30 nm and 100 nm layer of Cr deposited over the PDMS nanospheres with a Denton e-beam evaporator system. Due to the relatively poor step coverage of the e-beam evaporator, the sides of the PDMS nanospheres were not well covered by the Cr. The PDMS nanospheres were removed with CF<sub>4</sub> plasma along with the Cr on top of them, leaving behind the Cr hard mask on top of the Co/Pd multilayers. This Cr hard mask will serve as an etch mask for the ion milling. Figure 4.1 below shows a schematic of this process.

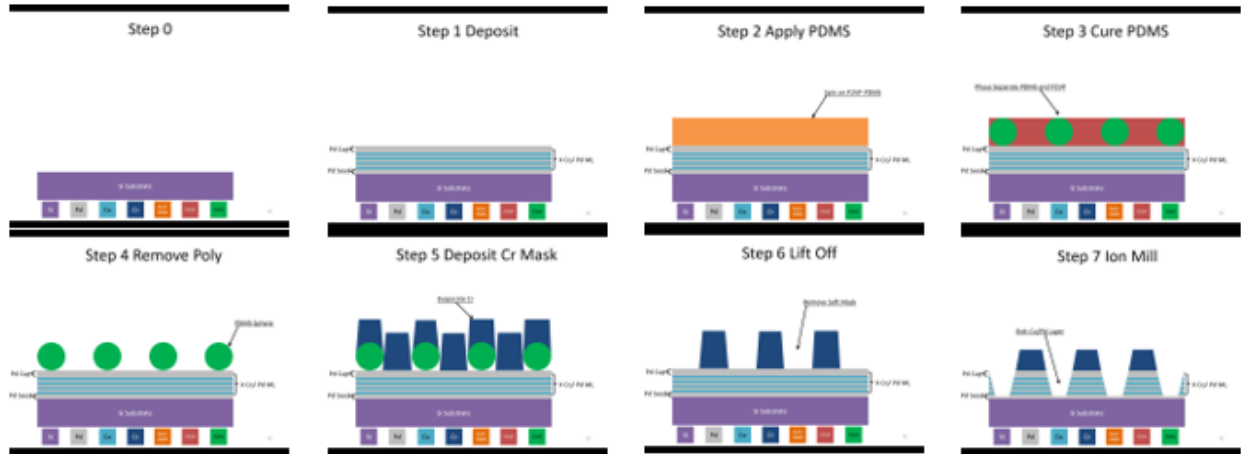


Fig. 4.1 Cr Hard Mask Process

Nanopillars formed by these two processes were characterized by magnetometry and SEM.

## 4.3 RESULTS AND DISCUSSION

### 4.3.1 P2VP-B-PDMS ETCH MASK

The full film out of plane M-H loop of the Pd 5 [Co 0.3/Pd 1.0]<sub>8</sub>/Pd 5 nm stack is shown in Figure 4.2 below. The Co/Pd film is perpendicular with a squareness ( $S^*$ ) of 0.6 and a coercivity ( $H_c$ ) of  $\sim 2.5$  kOe.

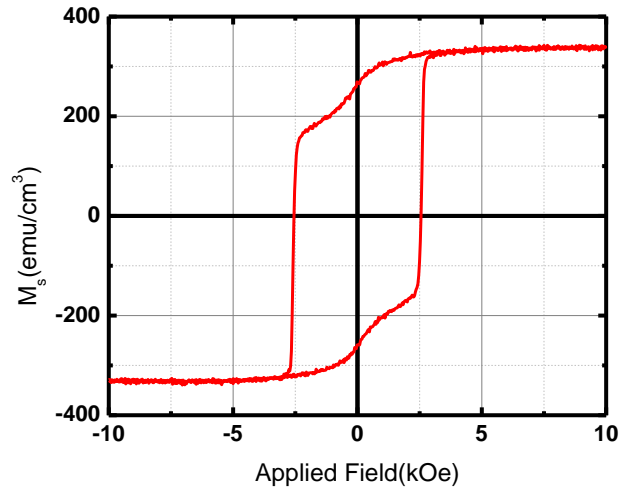


Fig. 4.2 Full film out of plane M-H loop of Pd5 [Co0.3Pd1.0]<sub>8</sub>Pd 5 nm thin film.

A matrix was completed with etch angles of  $60^\circ$ ,  $70^\circ$ , and  $80^\circ$  and etch times ranging from 5 to 30 sec with a beam voltage of 200 V. The magnetic characteristics for these samples showed that these etch times resulted in degradation of the magnetic thin film. Figures 4.3, 4.4, and 4.5 below show the compared M-H loops for all the etch angle sets of the matrix. Another matrix was completed, with the same etch angles as before, but with etch times from 1-4 secs and a beam voltage of 100 V in order to better control the etch rates of the samples.

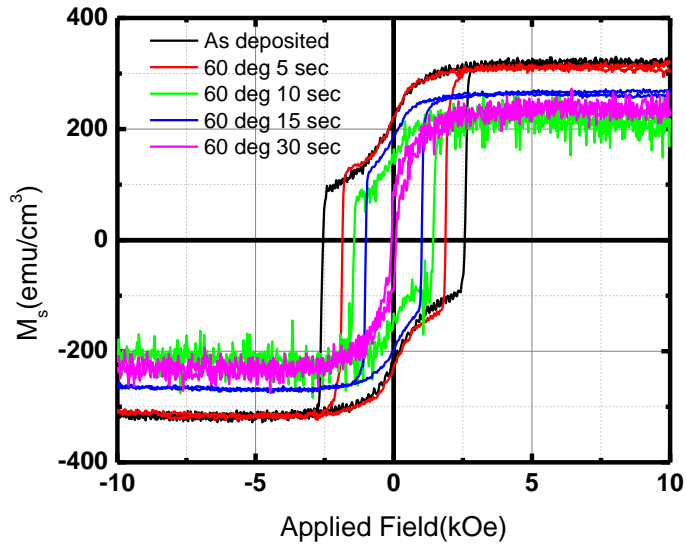


Fig. 4.3 Out of plane M-H loops for samples etched at  $60^\circ$  for 5-30 sec at 200 V beam voltage.

As we can see in Figure 4.3, at an etch angle of  $60^\circ$ , the coercivity steadily decreases as the etch time increases from 5 sec to 30 sec. Etching beyond 30 sec for all the samples results in more degradation of the magnetic thin film to the point at which there is no thin film remaining. Figure 4.4 shows the M-H loops for the  $70^\circ$  etch angle for etch times of 5-30 sec. The coercivity also decreases as the etch time increases, as for the  $60^\circ$  series.

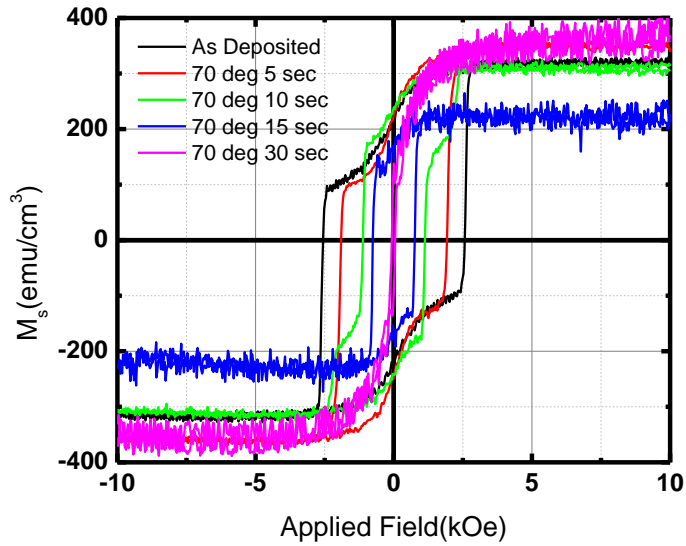


Fig. 4.4 Out of plane M-H loops for samples etched at 70° for 5-30 sec at 200 V beam voltage.

The 80° series in Figure 4.5 shows the same degradation of the coercivity as the etch time increases.

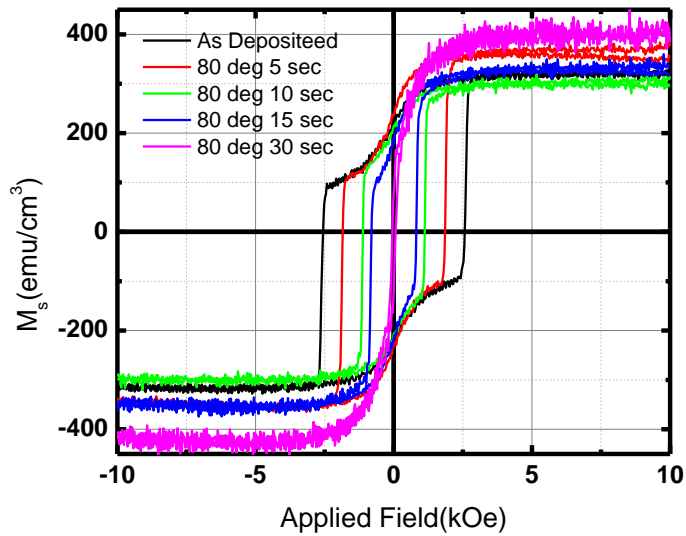


Fig. 4.5 Out of plane M-H loops for samples etched at 80° for 5-30 sec at 200 V beam voltage.

Etching at  $60^\circ$  at a beam voltage of 100 V for 1-4 sec yielded the greatest increase in coercivity, with a maximum coercivity of  $\sim 2.9$  kOe after etching at  $60^\circ$  for 2 sec. Figure 4.6 shows the out of plane M-H loops for all the samples etched at  $60^\circ$  for 1-4 secs.

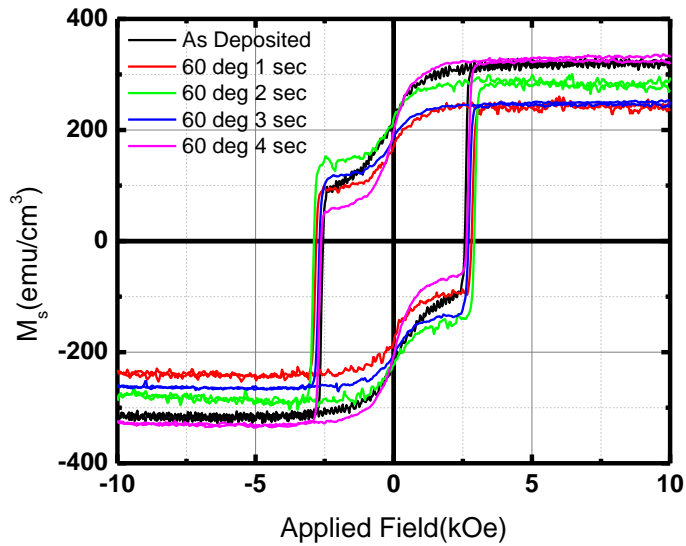


Fig. 4.6 Out of plane M-H loops for samples etched at  $60^\circ$  for 1-4 sec at 100 V beam voltage.

Similar results were found with the series of samples etched at  $70^\circ$  for 1-4 secs, except the increase in coercivity for the sample etched at  $70^\circ$  for 4 sec resulted in a coercivity of  $\sim 2.64$  kOe. Figure 4.7 shows the out of plane M-H loops for all the samples etched at  $70^\circ$  for 1-4 secs.

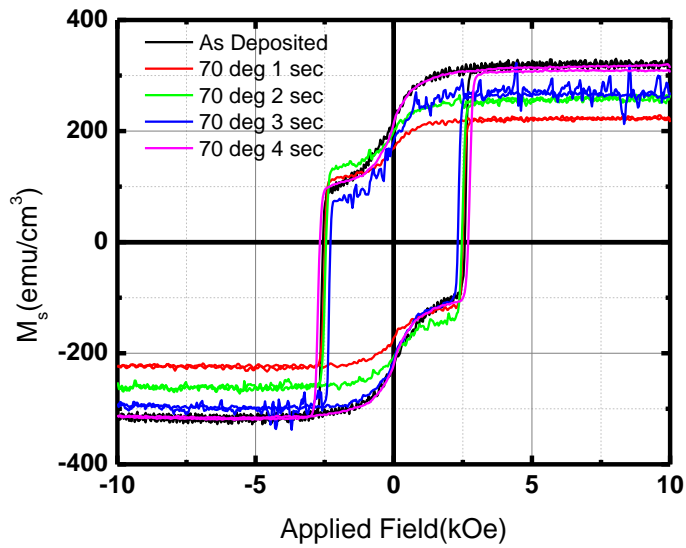


Fig. 4.7 Out of plane M-H loops for samples etched at  $70^\circ$  for 1-4 sec at 100 V beam voltage.

Etching at  $80^\circ$  for 1-4 sec has similar results for changes in coercivity as the samples etched at  $70^\circ$ , with a maximum coercivity of  $\sim 2.69$  kOe after etching at  $80^\circ$  for 3 sec at a beam voltage of 100 V. Figure 4.8 shows the out of plane M-H loops for the set of  $80^\circ$  etch angle samples.

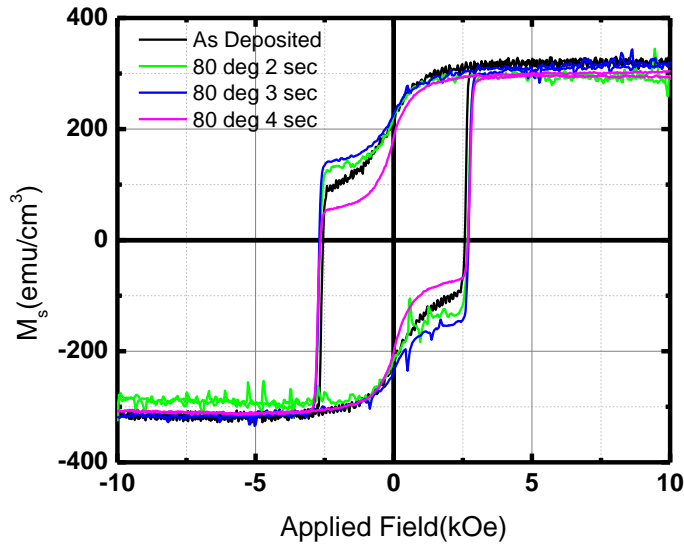


Fig. 4.8 Out of plane M-H loops for samples etched at 80° for 1-4 sec at 100 V beam voltage.

Examining the samples before ion beam etching and after etching at 60° for 1 and 2 sec, we find that the average diameter of the PDMS nanospheres is ~16.9 nm. Figure 4.9 shows SEM micrographs of the as deposited samples and after ion beam etching at 60° and 1 and 2 sec of etching. After ion beam etching for 1 sec, we find that the size of the nanopillars produced has decreased significantly, and after 2 sec, the nanostructures have become so minute, they are difficult to see. However, the magnetometry indicates the media has been patterned.

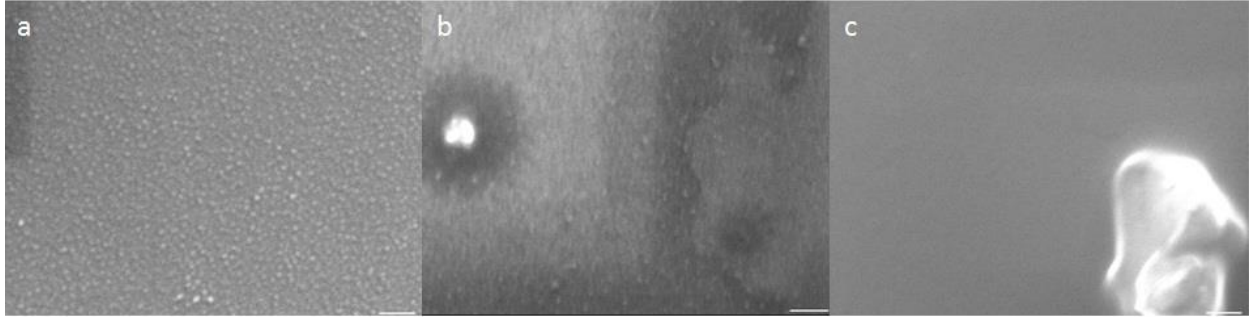


Fig. 4.9 SEM micrographs showing samples (a) As deposited and after etching at (b) 60° for 1 sec (c) 60° 1 sec.

Initially, we used a matrix with etch angles of 60°, 70° and 80° with etch times of 5, 10, and 15 sec, keeping the beam voltage set to 200V, then we extended the etch time to 30 and 45 sec. Extracting the coercivity data from Figures 4.3-4.5 and plotting the resulting data in Figure 4.10, we see that the coercivity decreases significantly at these etch conditions.

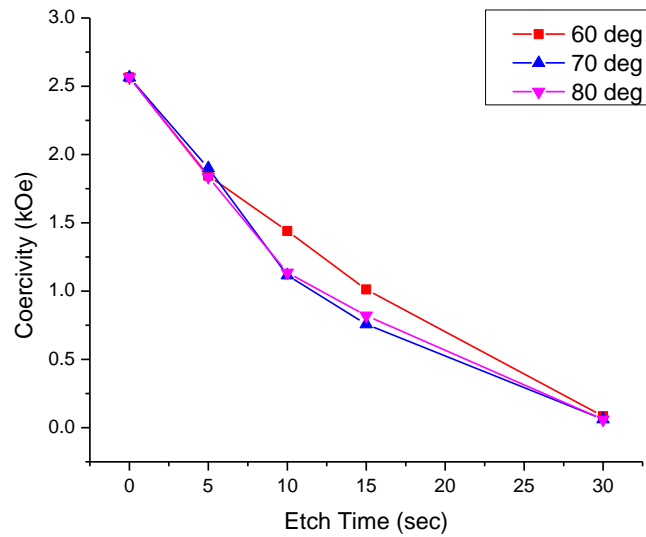


Fig. 4.10 Etch Time vs coercivity for etch angles of 60°-80° etched at 200 V.

Summarizing the results seen in Figure 4.6, we see that the coercivity increases from ~2.5 kOe to ~2.9 kOe, a ~15% increase, indicating that the magnetic media is patterned into magnetic islands. Figure 4.11 below plots the extracted coercivity versus etch time

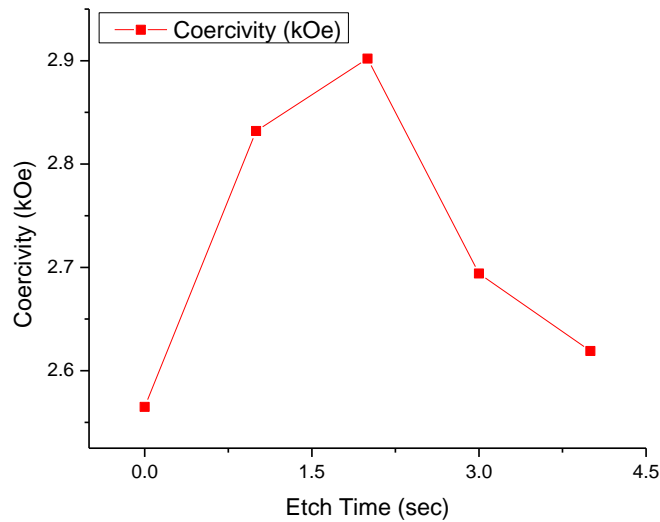


Fig. 4.11 Etch time vs. coercivity for etch angle of 60° etched at 100 V.

Further summarizing the results of the matrix study, Figure 4.12 plots the coercivity versus etch time for an etch angle of 70°. The coercivity also increased to ~2.6 kOe, a ~5% increase.

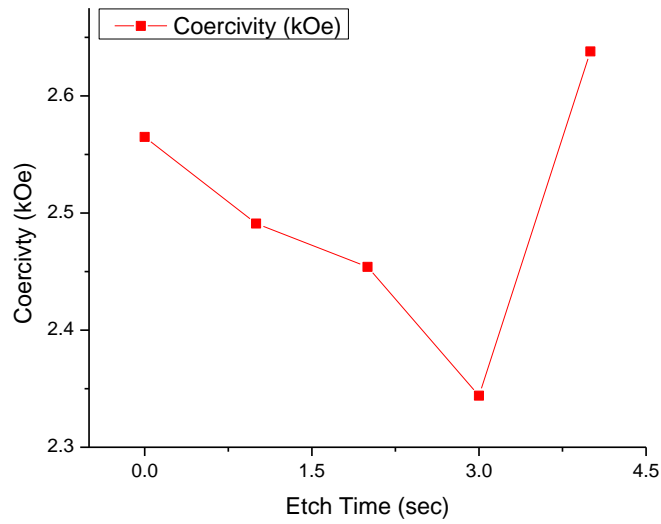


Fig. 4.12 Etch time vs. coercivity for etch angle of 70°.

Extracting the coercivity information from the M-H loops in Figure 4.8, we can see that the coercivity increased to a maximum of ~2.7 kOe after etching for 3 sec. Figure 4.13 is the extracted coercivity data versus etch time for the 80° series, and the coercivity increased to a maximum of ~2.7 kOe after etching for 3 sec.

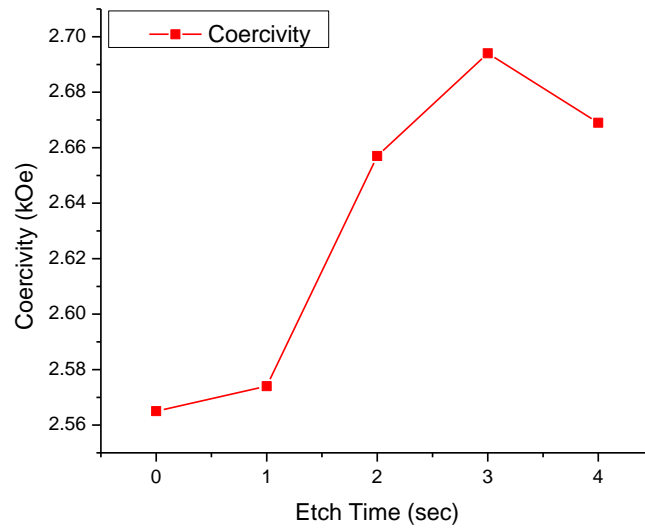


Fig. 4.13 Etch time vs. coercivity for etch angle of 80°.

Taking all the data from the M-H loops and creating a contour plot using MiniTab™ of coercivity vs etch angle and time, seen in Figure 4.14 below, we see that maximum coercivity can be produced with an etch angle of between 50°-60° and an etch time of ~2 sec. The SFD for the etched samples was calculated and plotted in figure 4.16 below.

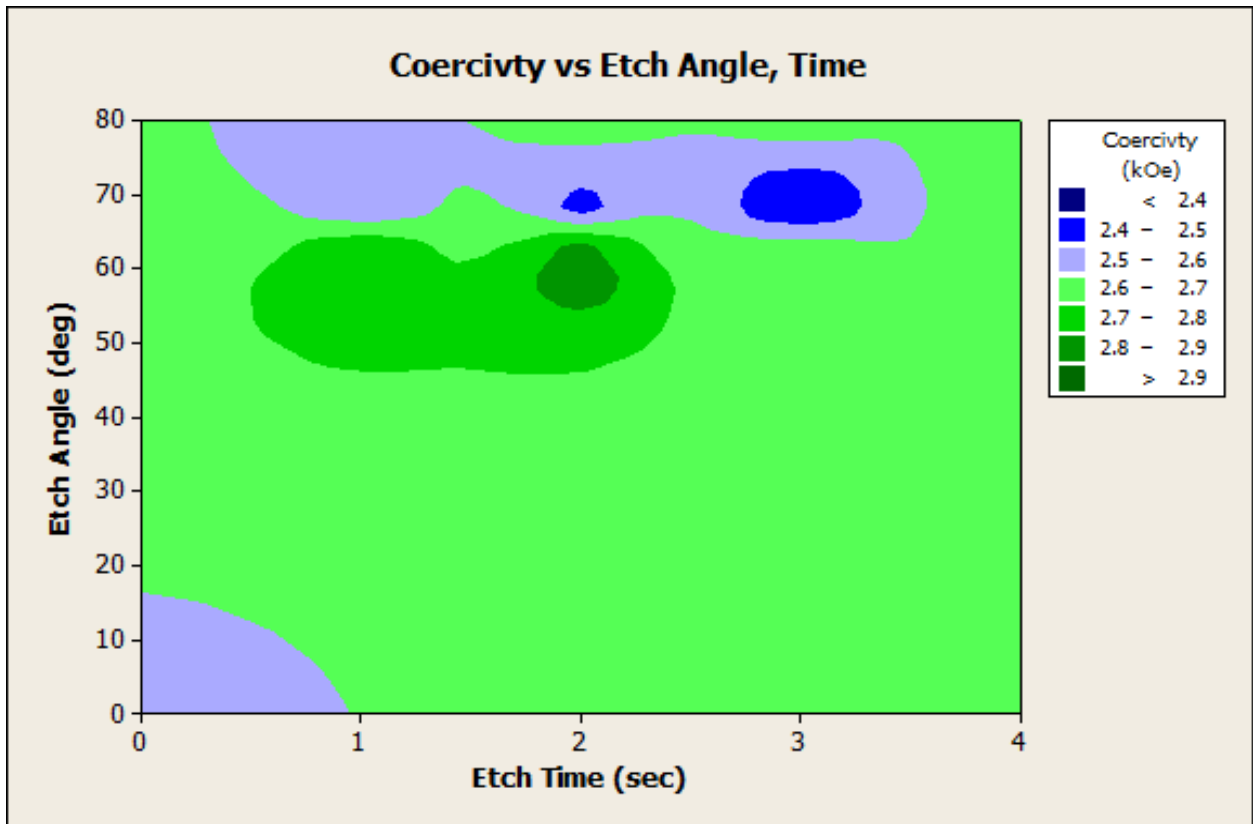


Fig. 4.14 Contour plot of coercivity vs. etch angle and time.

Plots of the SFD versus etch time are shown in Figure 4.15 below.

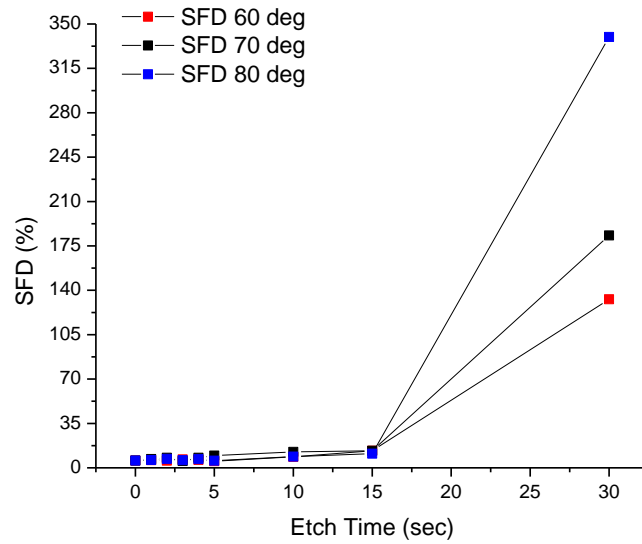


Fig. 4.15 SFD vs Etch time

The SFD for the full film sample was found to be 5.68%, indicating that the domains are probably switching at the same field. Figure 4.16 below shows the M-H loop for the sample etched at 60° and 2 secs and has a coercivity of 2.9kOe.

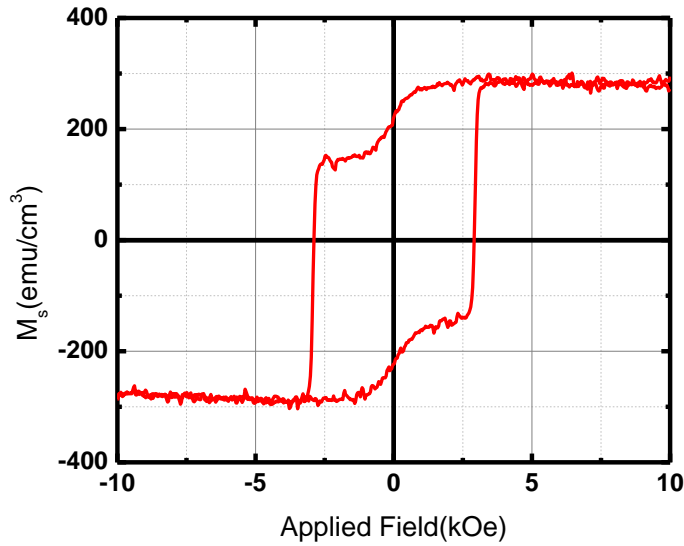


Fig. 4.16 M-H loop of sample etched at 60° for 2 sec.

The SFD was calculated as for the etched sample in Fig. 4.16 and is found to be 5.65%, very similar to the SFD for the as deposited sample.

Typically, as the magnetic islands decrease in size the SFD broadens<sup>53</sup>. Here the SFD is still very narrow, indicating that the magnetic islands are large or that the thin film has not been patterned significantly. Indeed, the SFD for the etched samples and the as deposited sample are effectively the same. However, the coercivity did increase with etching time to a maximum of ~2.9 kOe, indicating that some media patterning took place. We would expect to see some broadening of the SFD as the magnetic thin film was patterned.

#### 4.3.2 100 NM CR HARD MASK

100 nm of Cr was evaporated onto the Co/Pd-sputtered wafer and coated with plasma treated P2VP-b-PDMS block copolymer. After the Cr deposition, O<sub>2</sub> plasma was used to remove the PDMS nanospheres and the Cr layer on the nanospheres, as seen in Figure 4.1, above. After

ion milling at an angle of  $70^\circ$  for 1 min, the hysteresis loop, shown in Figure 4.17, shows a change in squareness, though there is no significant change in coercivity.

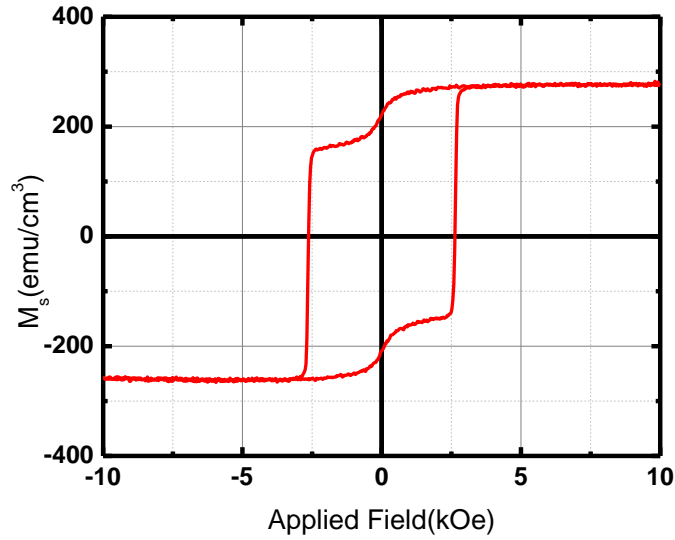


Fig. 4.17 M-H loop after etching 1 min at  $70^\circ$ .

A series of etches were made from 15 sec to 10 min. The resulting M-H loops are shown in Figure 4.18 below. As the ion milling proceeds, the coercivity does not change significantly, until the sample has been ion milled for 10 minutes. At that point, we start to see the coercivity decrease, indicating that the magnetic film has begun to be etched away. The squareness tends to decrease as the ion milling proceeds, while the SFD broadens considerably Figure 4.19 below plots coercivity, squareness and SFD for reference.

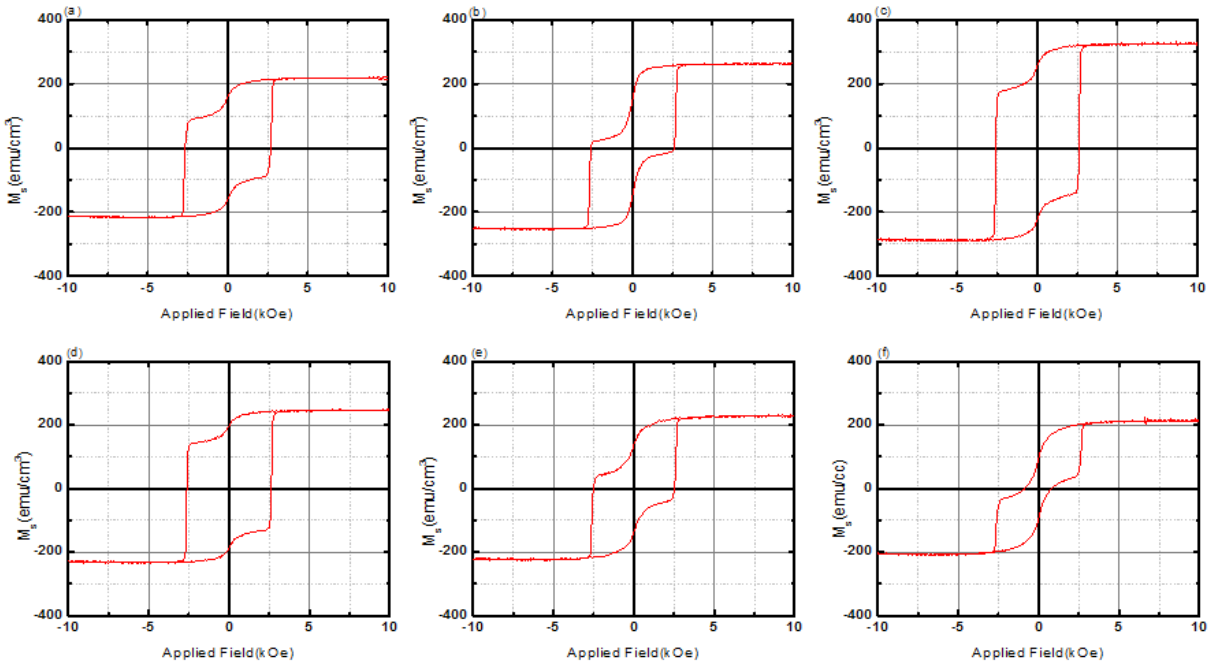


Fig. 4.18 Series of M-H loops after etching at 70° for (a) 15 sec (b) 30 sec (c) 45 sec (d) 60 sec (e) 5 min and (f) 10 min.

We can see in Figure 4.19 below that a after a minute of etching, there is not a discernable pattern forming, while after 5 minutes of etching, a slight pattern has formed. The squareness of the corresponding M-H loop has decreased, while the coercivity did not change significantly, until significant etching occurred, suggesting the material was being etched away.

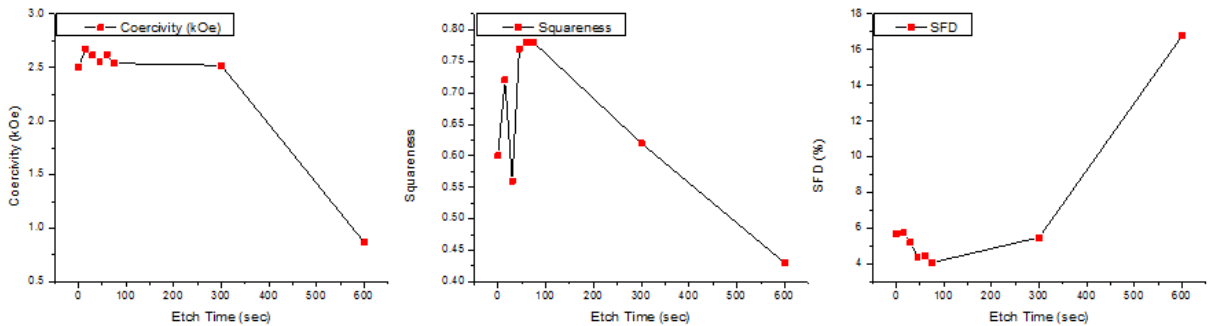


Fig. 4.19 Coercivity, squareness, SFD vs etch time for samples with 100 nm etched at 70°

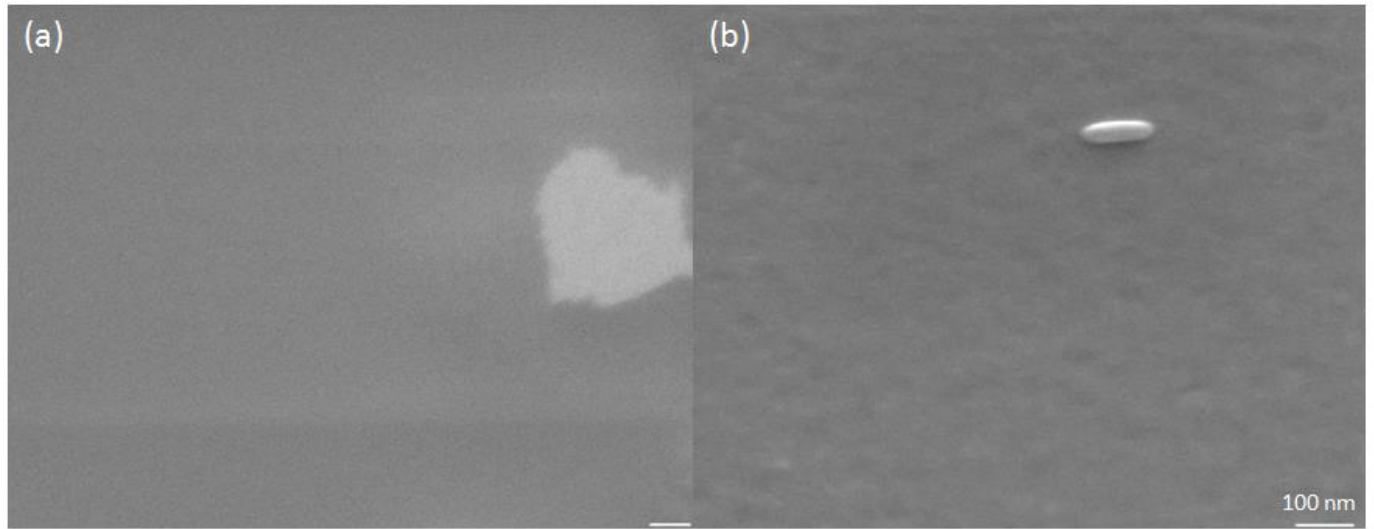


Fig. 4.20 SEM micrographs of 1000 Å Cr after etching at 70° for (a) 1min (b) 5 min.

#### 4.3.3 30 NM CR HARD MASK

The 30 nm Cr layer was ion milled at 70° and 80°, for 45, 60 and 75 sec. Magnetometry results are shown in Figure 4.21 below, and coercivity, squareness, and SFD have been extracted and are shown in Figures 4.22 and 4.23 below. We can see that the coercivity increased slightly, and there was a concurrent increase in squareness and SFD for samples etched at 70°.

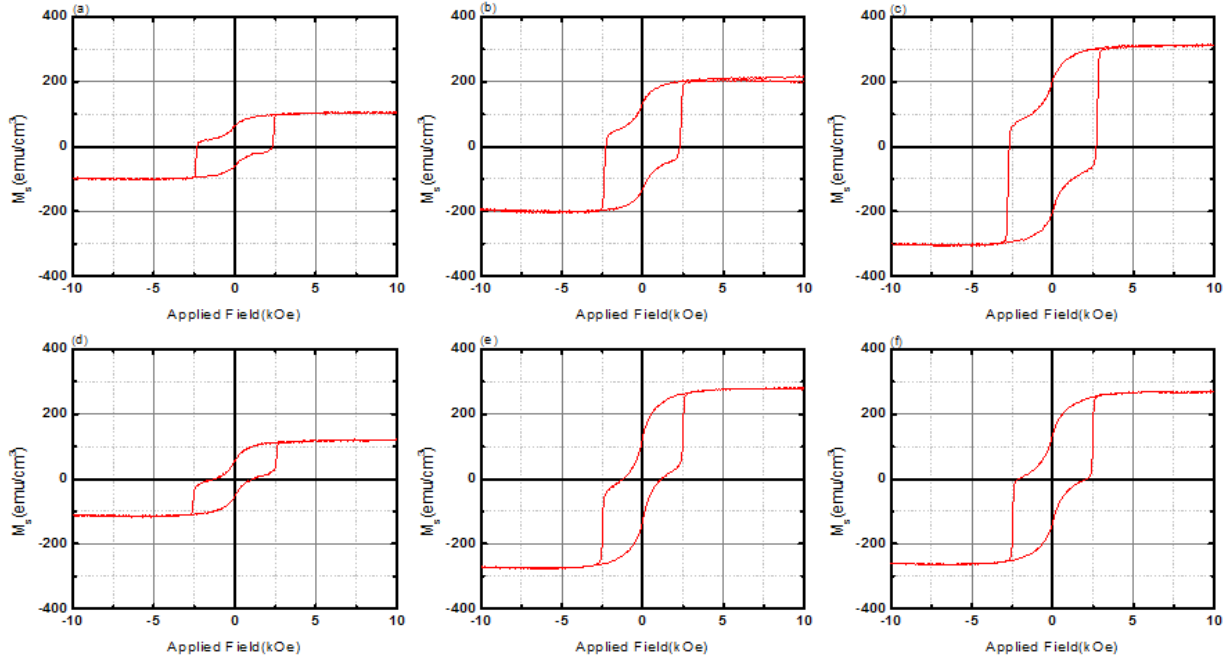


Fig. 4.21 M-H loops of Pd5[Co0.3Pd1.0]Pd 5 nm magnetic stack with P2VP-PDMS and 30 nm Cr coat ion milled at 70° for (a) 45 sec, (b) 60 sec, (c) 75 sec and ion milled at 80° for (d) 45 sec, (e) 60 sec and (f) 75 sec.

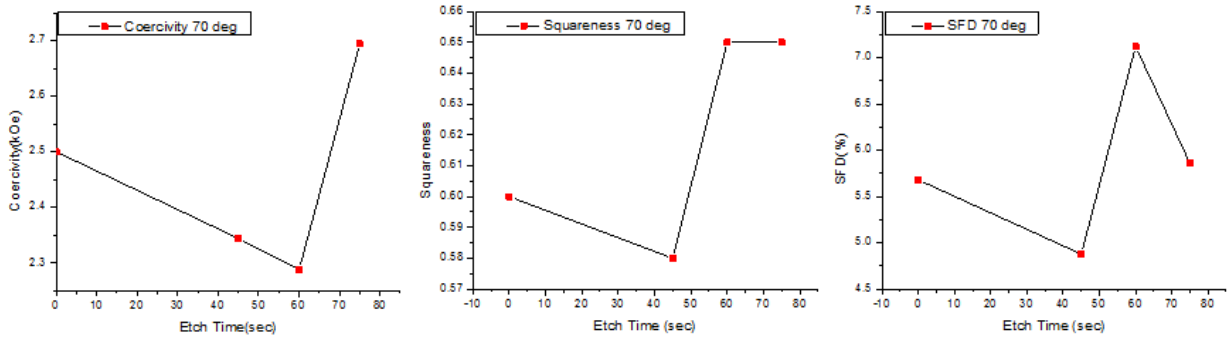


Fig. 4.22 Coercivity, squareness and SFD for samples with 30 nm Cr, etched at 70°.

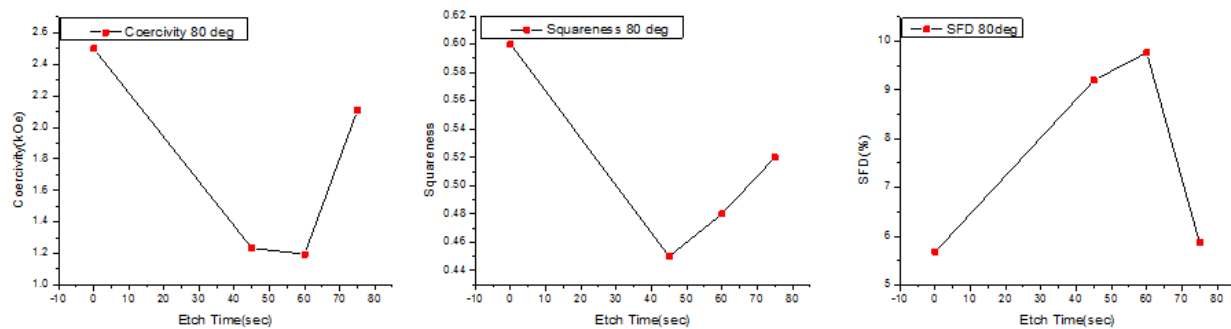


Fig. 4.23 Coercivity, squareness and SFD for samples with 30 nm Cr, etched at 80°

The results for samples etched at  $80^\circ$ , we can see in Figure 4.23 that the coercivity and squareness decreased with increased etching time, while the SFD broadened considerably. SEM imaging did not reveal nanopillars. This suggests that the changes in coercivity and squareness were a result of either ion irradiation<sup>69,70</sup> damage or removal of material from the substrate.

#### 4.3.4 20 NM CR HARD MASK

A 20 nm layer of Cr was deposited onto the wafer in the same way as the 100 nm and 30 nm Cr layer previously described. Samples were etched at  $60^\circ$ ,  $70^\circ$  and  $80^\circ$  for 45, 60 and 75 sec. Magnetometry results are in Figure 4.24 below. Again, the coercivity, squareness and SFD have been extracted and are plotted in Figures 4.25, 4.26, and 4.27 below for the etch angles of  $60^\circ$ ,  $70^\circ$  and  $80^\circ$ .

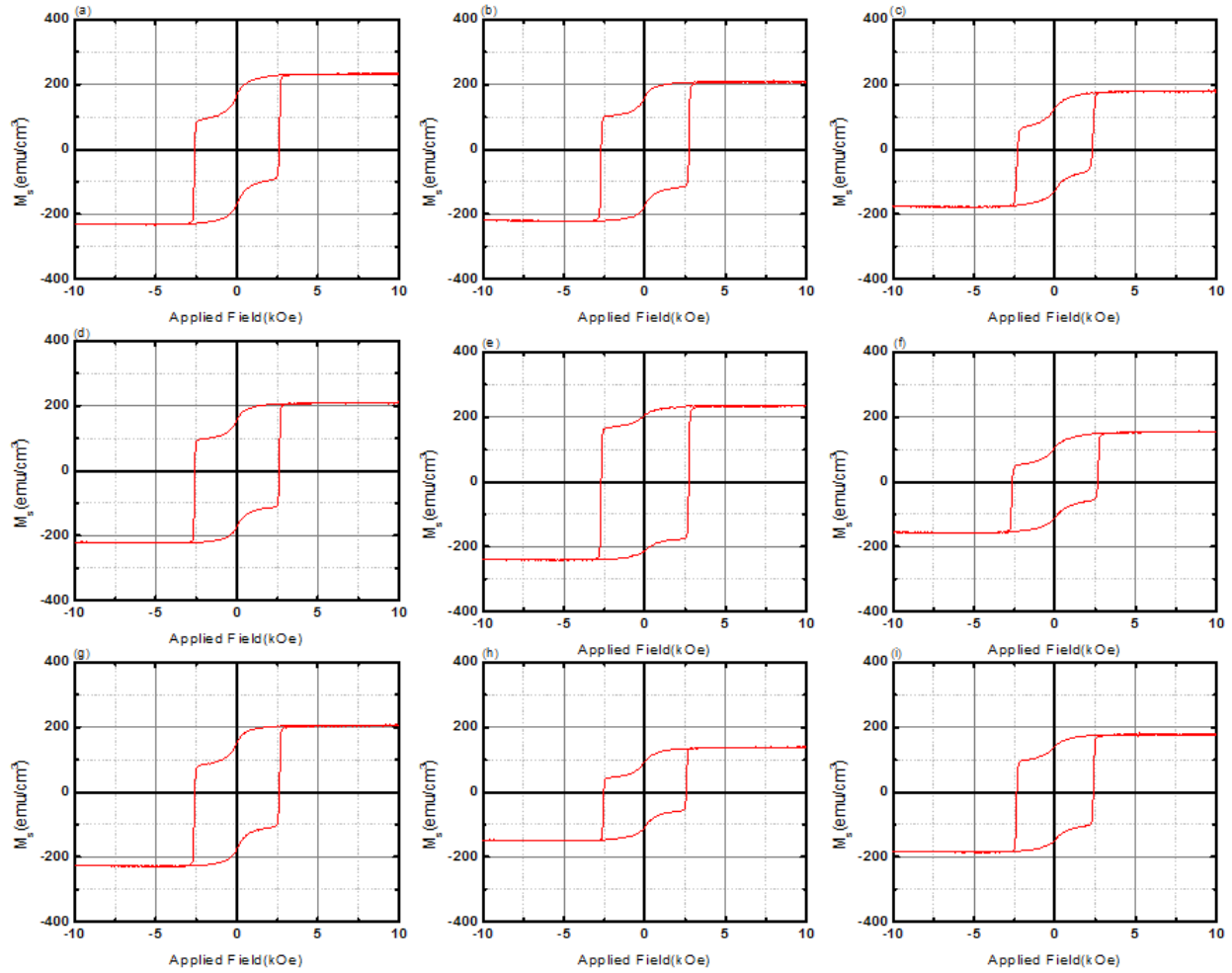


Fig. 4.24 M-H loops of Pd<sub>5</sub>[Co<sub>0.3</sub>Pd<sub>1.0</sub>]Pd 5 nm magnetic stack with P2VP-PDMS and 20 nm Cr coat ion milled at 60° for (a) 45 sec, (b) 60 sec, (c) 75 sec and ion milled at 70° for (d) 45 sec, (e) 60 sec and (f) 75 sec and ion milled at 80° for (g) 45 sec, (h) 60 sec and (i) 75 sec.

As we can see in Figure 4.25, coercivity increased slightly to a maximum of ~2.7 kOe with squareness increasing concurrently, while SFD generally broadened with etch time.

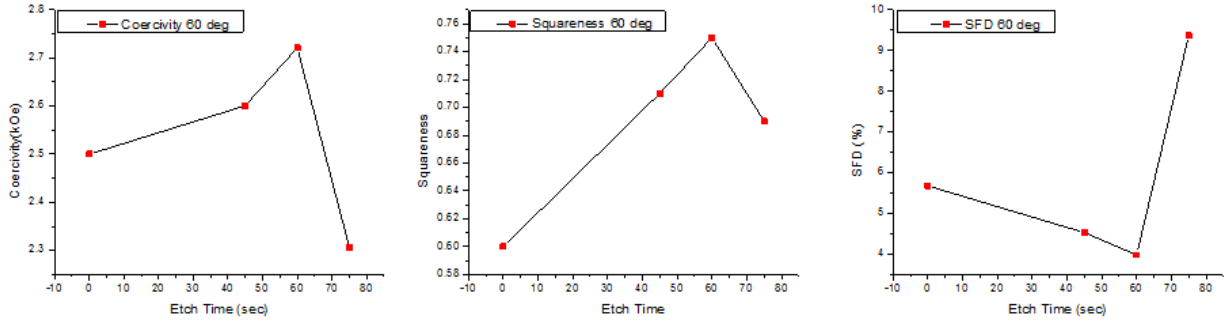


Fig. 4.25 Coercivity, squareness and SFD for samples with 20 nm Cr, etched at 60°.

Samples with 20 nm Cr and etched at 70° show very similar trends as for the samples etched at 60°, as can be seen in Figure 4.26 below.

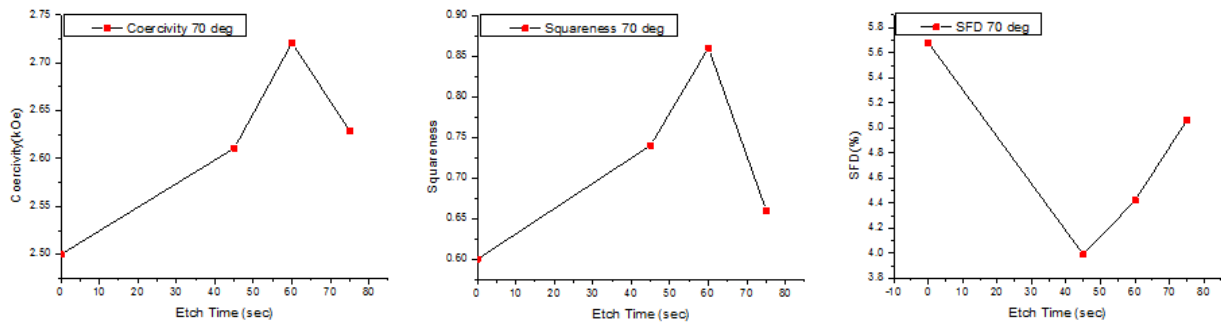


Fig. 4.26 Coercivity, squareness and SFD for samples with 20 nm Cr, etched at 70°.

Samples with 20 nm Cr and etched at 80° show a decreasing trend with coercivity, but similar trends for squareness and SFD, seen in Figure 4.27 below.

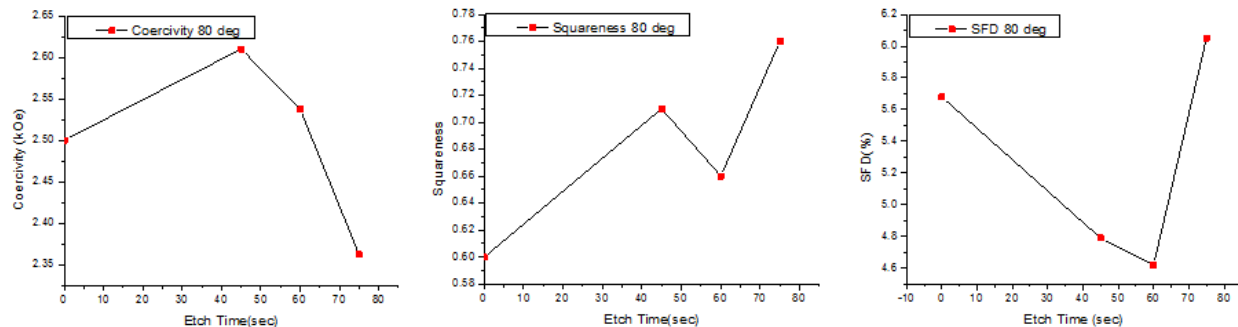


Fig. 4.27 Coercivity, squareness and SFD for samples with 20 nm Cr, etched at 80°.

SEM imaging again revealed no nanopillars for this set of samples, suggesting that the changes in magnetic characteristics is also the result of damage from ion irradiation.

#### 4.4 CONCLUSIONS

We coated magnetic thin films with P2VP-PDMS block copolymer, and then evaporation deposited 100, 30 and 20 nm of Cr on top of the samples. Evaporation generally has poor step coverage, and it was believed that using a CF<sub>4</sub> plasma would remove the PDMS nanospheres, lifting off the Cr, leaving behind a hard mask. The samples were etched in an ion mill with a variety of etch angles and times. The magnetic characteristics and SEM images suggest that the plasma ashing to lift off the Cr was not successful. A possible reason would be the thickness of the deposited Cr was too great, and therefore the plasma did not remove the PDMS nanospheres. A possible solution might be trying a thinner Cr layer or a different block copolymer.

## 5. NANOPATTERNING MAGNETIC MEDIA USING ULTRASONIC SIZE TUNED BLOCK COPOLYMERS

### 5.1 INTRODUCTION

This chapter introduces a method to shrink block copolymer nanospheres in order to produce a high areal density patterned magnetic thin film. Since survivability of the block copolymer is an issue, PS-b-PFS was chosen due to its superior survivability compared to P2VP-b-PDMS block copolymer. PS is an organic and is highly soluble in toluene as noted previously; however, PFS tends to segregate from toluene. However, PFS does contain some organic components in addition to Fe and Si. Owing to the adage from chemistry, “like dissolves like”, it was believed that subjecting a sample with PFS nanospheres to an ultrasonic process while in a toluene bath may result in more organic components being dissolved, leaving behind smaller PFS nanospheres. A  $\text{Co}_{25}\text{Pd}_{75}$  alloy was selected due to its high full film coercivity and squareness, determined from experiment.

### 5.2 EXPERIMENTAL DETAILS

A stack consisting of Ta5/Pd5/ $\text{Co}_{25}\text{Pd}_{75}$ 20/Ta5 nm was sputter deposited onto a 3” Si wafer using a SFI Shamrock sputtering system with an Ar + pressure of 2 mTorr and then *in situ* annealed at 400°C for 8 min. A 1.5 wt % solution of PS-b-PFS, identical to the block copolymer used in previous chapters was dissolved in toluene and spin-coated at 4000 rpm for 40 sec onto the wafer with the CoPd alloy<sup>57,60,73</sup>. The wafer was then baked at 140°C for 48 hrs. to phase separate the

PS into a matrix containing PFS nanosphere; the PS matrix was removed with oxygen plasma as previously discussed<sup>57</sup>. In order to remove/size tune the PFS, samples with CoPd alloy and PFS nanoparticles were placed in a toluene bath and subjected to ultrasonic cleaning for 2 hrs<sup>74</sup>. The ultrasonic process was performed in 0.5 hr. intervals to minimize heating. After the ultrasonic bath, the samples were ion milled in argon to etch<sup>57,60</sup> the CoPd alloy film. From prior results, it was decided to maintain a constant etch angle of 55° to yield an optimal coercivity, with etch times ranging from 30 sec to 2:45 min.

### 5.3 RESULTS AND DISCUSSION

The full film Ta5/Pd5/Co<sub>25</sub>Pd<sub>75</sub>20/Ta5 nm out-of-plane M-H loop is shown in Figure 5.1 below. The film is perpendicular with a coercivity and squareness of ~3.3 kOe and 0.93, respectively. The switching field distribution is 3.2%.

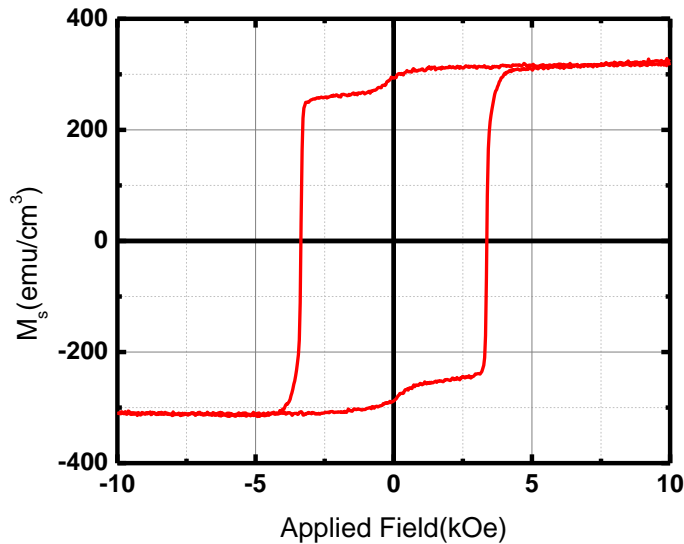


Fig. 5.1 Full film out-of-plane M-H loop of Ta5/Pd5/Co<sub>25</sub>Pd<sub>75</sub>20/Ta5 nm stack.

A SEM micrograph of the sonicated sample was taken and can be seen in Figure 5.2(a) below. The average diameter of the nanospheres was found to be  $\sim 10$  nm with a standard deviation of 0.5 nm. This yields a theoretical areal density of  $\sim 1250$  Gb/in<sup>2</sup>; however, etching will result in slightly larger nanopillars. After etching at 55° for 1:45 min, the average diameter of the nanopillars was found to be  $\sim 20$  nm, yielding an areal density of  $\sim 400$  Gb/in<sup>2</sup>.

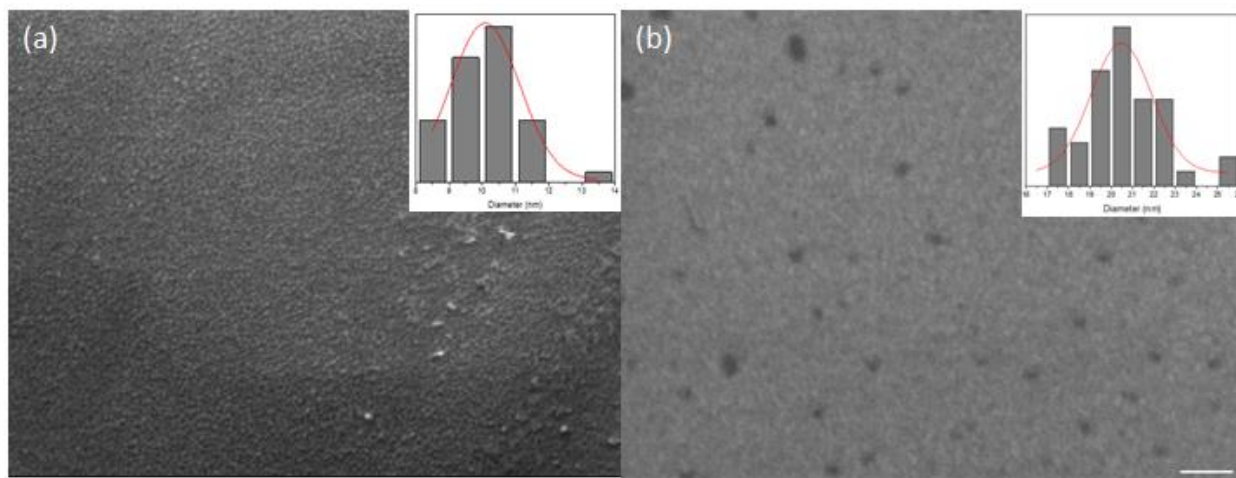


Fig. 5.2 SEM micrograph of PS-b-PFS nanospheres after (a) 2 hr. ultrasonic in toluene bath (b) etch 55° 1:45 min. Scale bar 100 nm.

After the ultrasonic process, samples were ion milled with etch parameters as discussed in the preceding section. The resulting M-H loops are in Figures 5.3 and 5.4 below.

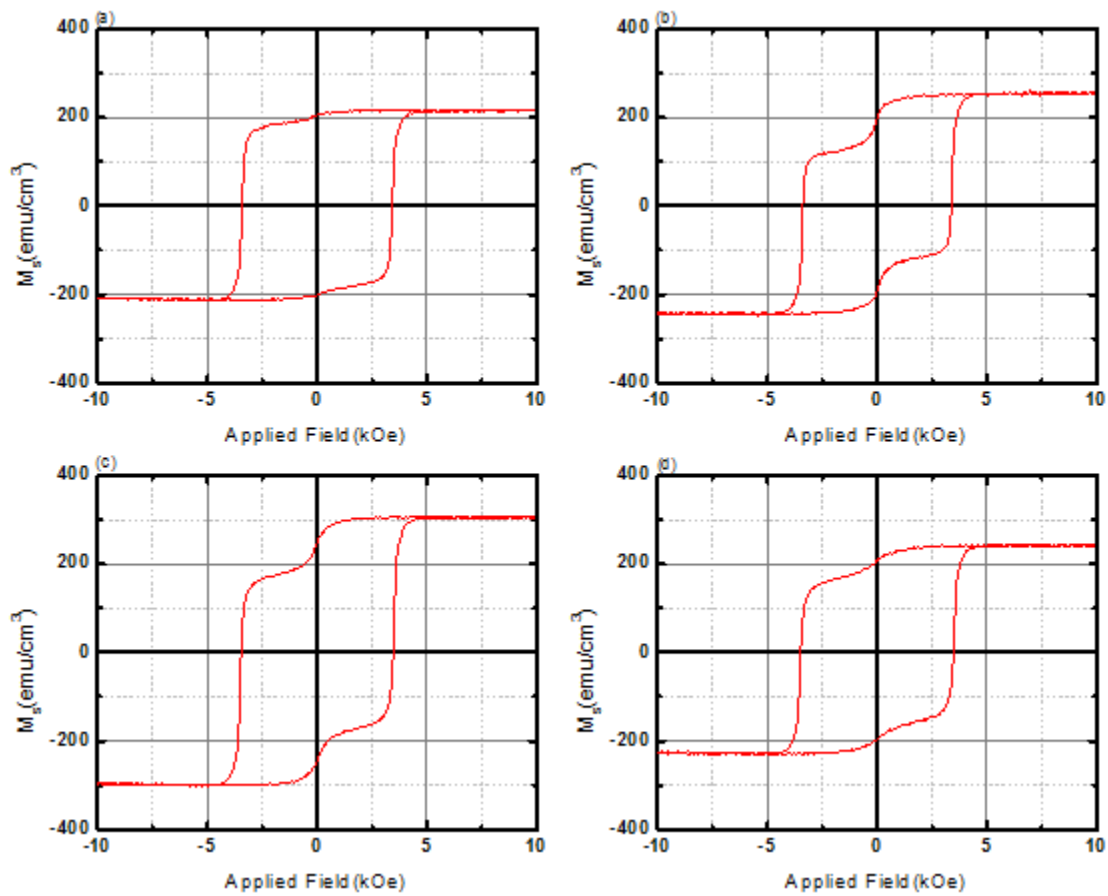


Fig. 5.3 Out-of-plane M-H loops of samples etch at  $55^\circ$  for (a) 30 sec (b) 45 sec (c) 1 min (d) 1:15 min.

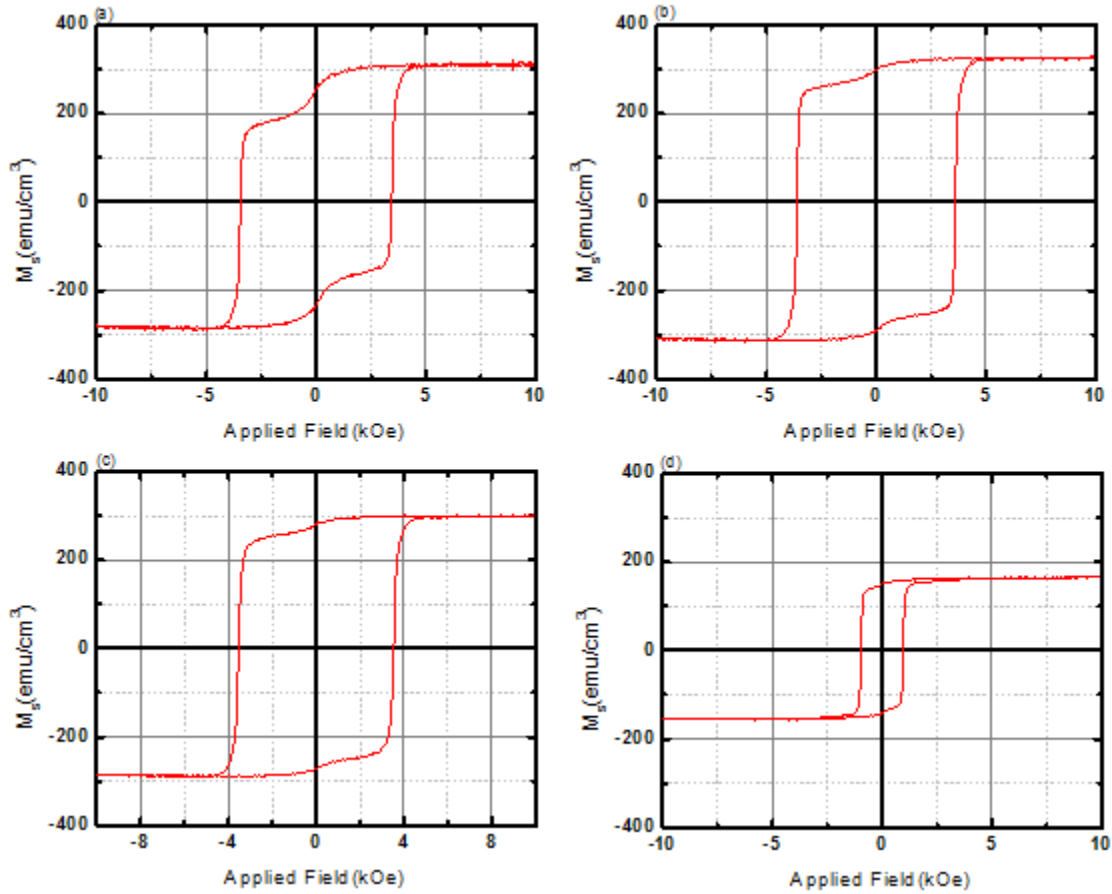


Fig. 5.4 Out-of-plane M-H loops of samples etch at  $55^\circ$  for (a) 1:30 min (b) 1: 45 min (c) 2 min (d) 2:45 min.

Magnetic characteristic data from Figures 5.3 and 5.4 was extracted and are plotted in Figure 5.5 below.

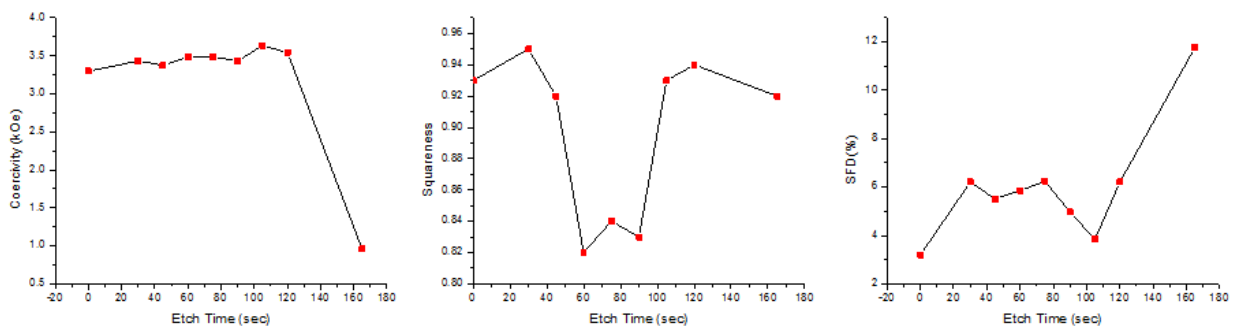


Fig. 5.5 Coercivity, squareness and SFD vs. etch time.

The coercivity was improved noticeably after etching for 1:45 min, while the squareness remained comparable to the full film squareness. The SFD for this etch parameter broadened slightly, but

is still less than 10%, comparable to pre-patterned pillars. For etching times beyond 2 min, the coercivity decreases, indicating material removal and possible ion irradiation<sup>69,70</sup> damage.

#### 5.4 CONCLUSIONS

A method of shrinking block copolymers to pattern magnetic thin films was attempted to achieve high areal density. The block copolymers were shrunk with a combination of ultrasound and a toluene bath. The ultrasonic process resulted in PFS nanospheres ~10 nm in diameter, with an areal density<sup>75</sup> of ~1250 Gb/in<sup>2</sup>. After etching, the patterned film yielded an areal density<sup>8</sup> of ~400 Gb/in<sup>2</sup>, however the pattern is difficult to see. A possible solution may be to attempt to improve the survivability of the PFS nanospheres, perhaps by coating the nanospheres with a metal, such as Cr.

## 6. FIRST ORDER REVERSAL CURVES STUDY OF PATTERNED MEDIA

### 6.1 INTRODUCTION

In order to gain some insight into the switching behavior of our patterned media, we employed First Order Reversal Curves (FORC). FORC is an experimental technique to study the internal switching behavior of magnetic materials. The FORC measurement is acquired using the AGM as described in section 2.3.1. At the beginning of the measurement, an applied field,  $H_{\text{sat}}$ , saturates the sample beyond the saturation magnetization,  $M_s$  of the sample. The applied field is decreased to a reversal field,  $H_r$ , where the field is then swept back to  $H_{\text{sat}}$  in  $H$  steps.  $H_r$  is increased by a regular, set value and the process is repeated until a set of FORC curves are collected. The magnetization at each point is measured, yielding  $M(H_r, H)$ . The set of FORC curves is used to calculate the FORC distribution  $\rho$  by taking a second order mixed partial derivative of  $M(H_r, H)$ , as given by Equation 6.1 below<sup>32-34</sup>.

$$\rho(H_r, H) = \frac{\partial^2 M(H_r, H)}{\partial H_r \partial H} \quad (6.1)$$

It is convenient to transform  $H$  and  $H_r$  to a coercive field  $H_c$  and a bias field  $H_b$  using equations 6.2 and 6.3 below.

$$H_c = \frac{(H - H_r)}{2} \quad (6.2)$$

$$H_b = \frac{(H + H_r)}{2} \quad (6.3)$$

This coordinate transformation tilts the axis at  $45^\circ$  to show the FORC distribution. The FORC distribution can be used as another method to see the switching field distribution, based on the location of the peaks in the plot. Coercivity can be determined based on where the peak is located on the  $H_c$  axis, and information about the width and breadth of the coercivity based on the width of the peak<sup>32-34</sup>. Note that FORC measurements only capture the irreversible portion of the magnetization curve, and purely reversible samples would not have a FORC distribution<sup>32-34</sup> (i. e. the mixed second order partial derivative is zero).

A pair of idealized hysteresis loops and their FORC distributions is shown in Figure 6.1 below. Idealized hysteresis loops with positive and negative bias are shown in Figures 6.1(a) and 6.1(b), respectively. The loops are idealized and are therefore represented by points; a realistic FORC distribution would be Gaussian.

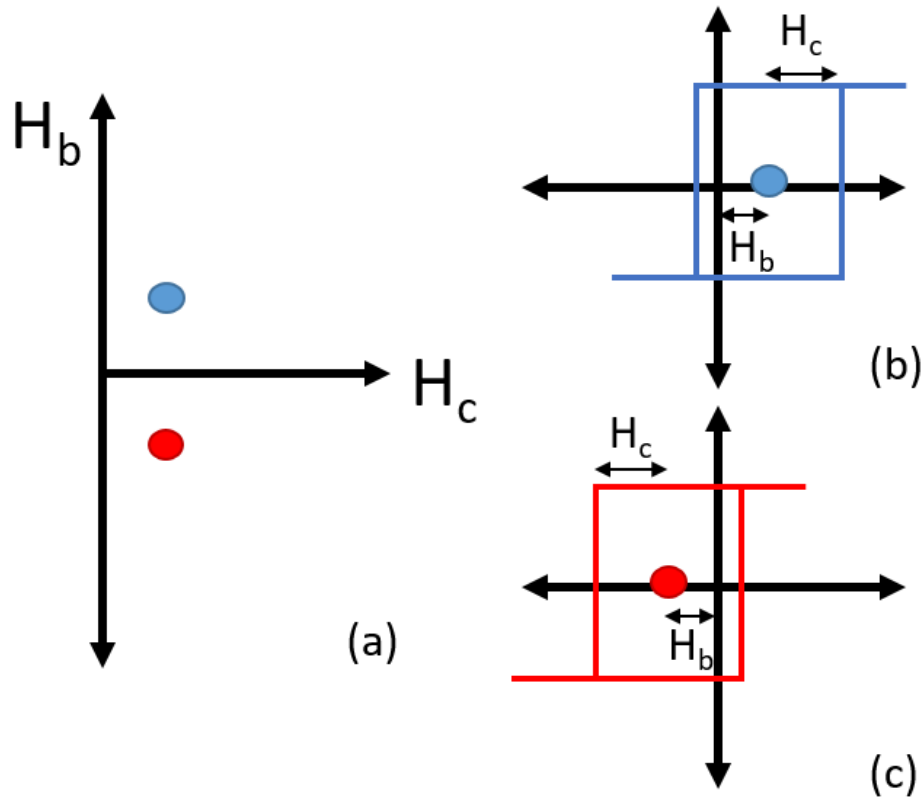


Fig. 6.1 Idealized FORC example (a) FORC distribution (b) positive bias M-H loop (c) negative bias M-H loop. Image courtesy B.D. Clark

As previously discussed, each FORC measurement consists of several FORC curves, which are evenly spaced by the AGM. A finite difference equation based on Equation 6.1 is used to calculate the FORC distribution (Equation 6.4).

$$\frac{\partial^2 M(H_r, H)}{\partial H_r \partial H} = M(A) - M(B) + M(C) - M(D) \quad (6.4)$$

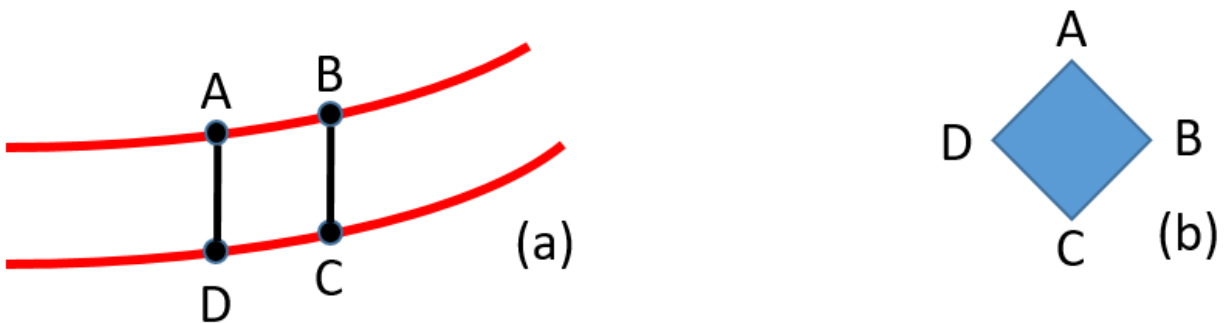


Fig. 6.2 (a) Point selection and interpolation (b) FORC calculation. Image courtesy B.D. Clark

In Figure 6.2(a), we see two FORC curves. Points A and B have been selected, and these have been interpolated to points C and D on the lower FORC curve. These points are used with Equation 6.4 to calculate the FORC distribution,  $\rho$ .

## 6.2 EXAMPLE FROM HEPTANE ANNEALING STUDY

In order to gain further insight into the switching behavior of our patterned media, we turned to FORC analysis. The first sample we chose to study is the heptane annealed sample seen in Figure 3.7(b), due to the “splitting” behavior of the M-H loop. Given that Equation 6.1 must be evaluated numerically, it is necessary to use software to aid our analysis. There are a number of software packages that have been developed for FORC analysis; we chose VARIFORC<sup>4</sup> due to the easy availability of Mathematica<sup>TM</sup> via the University of Alabama and FORC+<sup>5</sup>, developed by Dr. Pieter Visscher at the University of Alabama.

VARIFORC consists of a number of modules based off Mathematica<sup>TM</sup> that are used sequentially to calculate and plot the FORC distribution<sup>76</sup>. FORC+ directly calculates the FORC distribution without having to open different modules in sequence<sup>35</sup>. FORC+ also performs less

smoothing than VARIFORC, which helps preserve some information. Figure 6.3 below shows the VARIFORC analysis while Figure 6.4 below shows the FORC+ analysis.

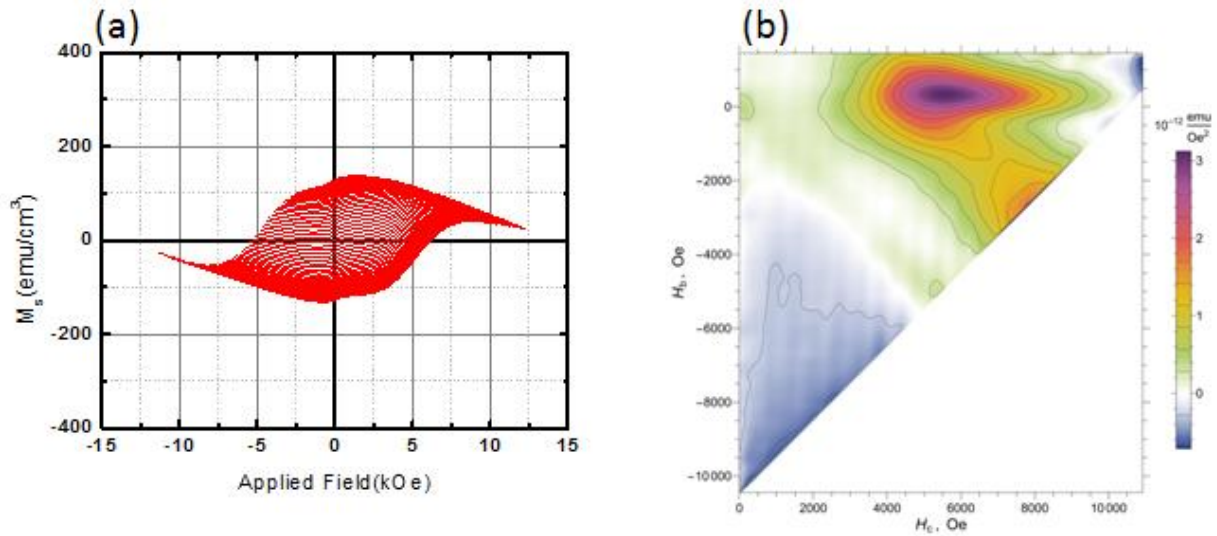


Fig. 6.3 (a) FORC curves and (b) VARIFORC distribution of heptane annealed sample etched at 45° 3.5 min.

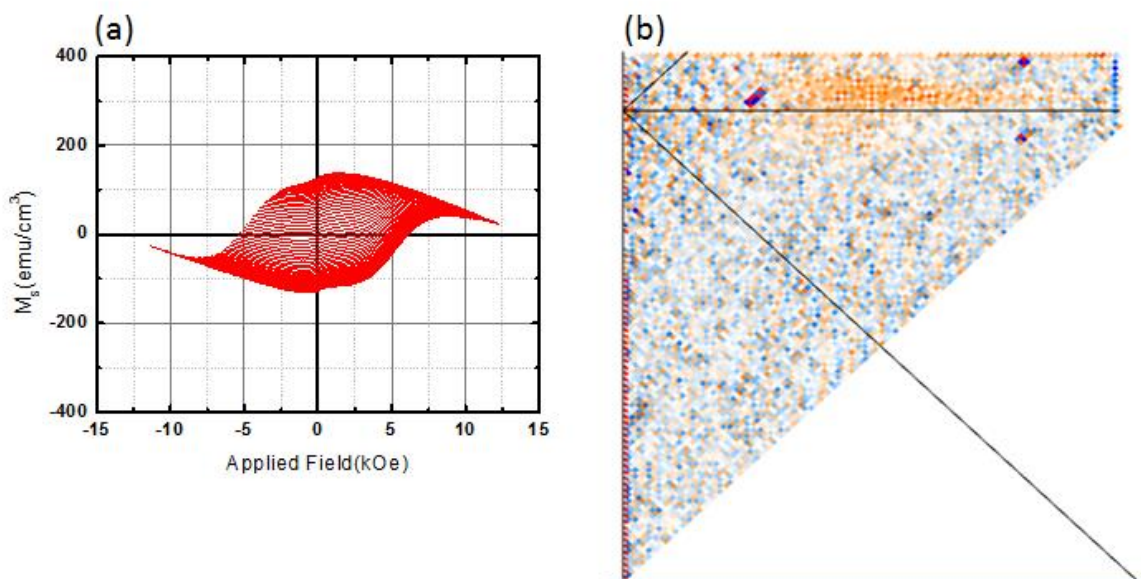


Fig. 6.4 (a) FORC curves and (b) FORC+ distribution of heptane annealed sample etched at 45° 3.5 min.

The VARIFORC distribution in Figure 6.3(b), the changes in the mixed second partial derivative are represented by color contour, while the changes in the same in FORC+ are represented by red-yellow “positive” change and blue “negative” change, with intensity of the color representing the magnitude of the partial derivative. The FORC distributions in Figures 6.3(b) and 6.4(b) are similar, both having a “ridge” in the direction of the  $H_c$  axis. Dumas, et al indicate that the ridge in a FORC distribution is similar to an assembly of single domain magnetic nanoparticles with little dipolar interactions<sup>36</sup>. The SEM in Figure 3.2(d) show a patterned film, with clearly separated nanostructures, correlating with the FORC distribution.

### 6.3 EXAMPLE FROM COPD ALLOY PATTERNING

Another example studied with FORC analysis is a sample of CoPd alloy patterned by ion milling from the previous Chapter 5. As before, we used both VARIFORC and FORC+ in our

study. Figures 6.5 and 6.6 show the FORC curves and FORC distributions produced from VARIFORC and FORC+, respectively. VARIFORC in this case produced a peak that is centered at  $\sim 3.6$  kOe, corresponding to the coercivity of the M-H loop seen in Figure 5.4(b). This might indicate that the switching mechanism is vortex switching, with larger non-single domains<sup>36</sup>.

However, there is no “ridge”, just the peak. However, FORC+ produced a “ridge” along the  $H_b$  axis. Since FORC+ performs little to no smoothing compared to VARIFORC, FORC+ is most likely more accurate. The ridge may indicate there is minimal interaction among any nanostructures on the sample<sup>36</sup>. The SEM micrograph in Figure 5.2(b) show very small nanostructures, again correlating with the FORC analysis.

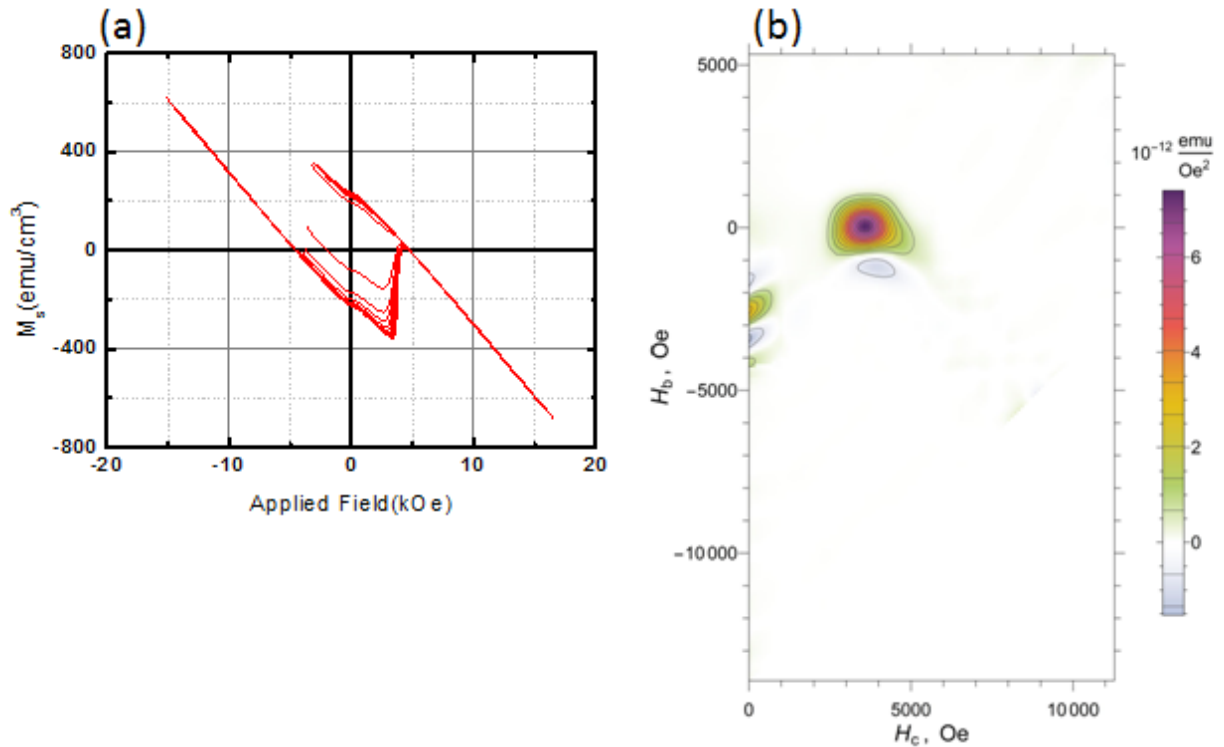


Fig. 6.5 FORC curves and (b) VARIFORC distribution of CoPd alloy sample etched at  $55^\circ$  1:45 min.

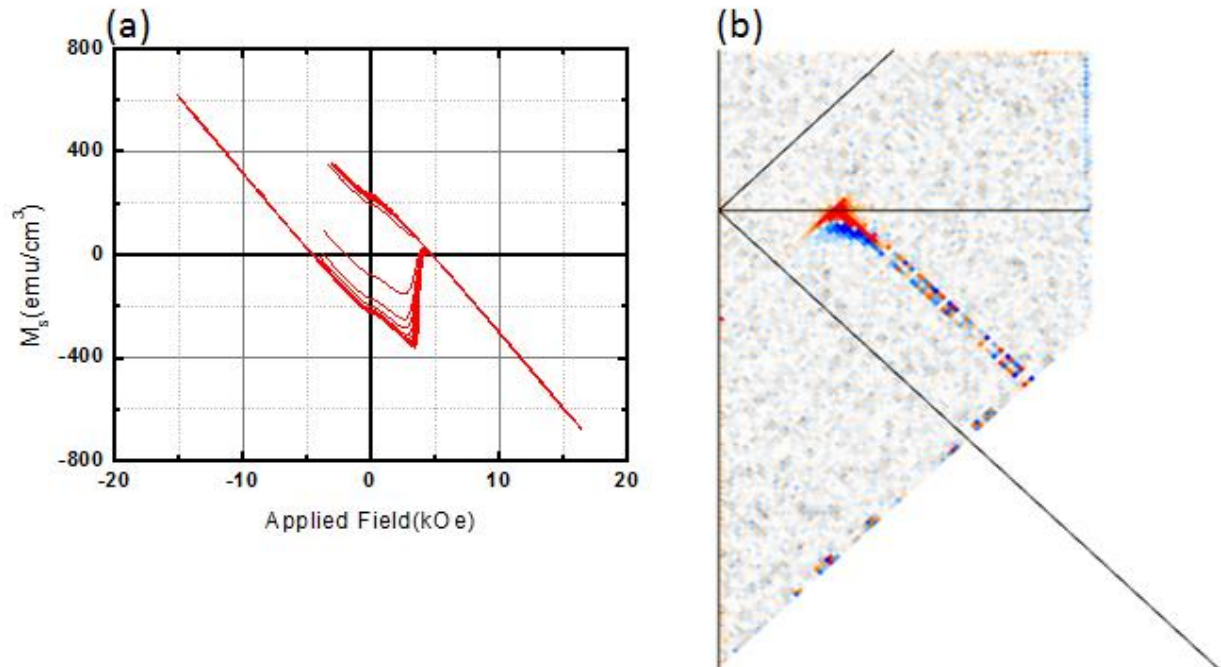


Fig. 6.6 FORC curves and (b) FORC+ distribution of CoPd alloy sample etched at  $55^\circ$  1:45 min.

#### 6.4 CONCLUSIONS

Analysis using FORC was carried out on a variety of samples to study the switching behavior of the patterned magnetic thin film. FORC analysis was carried out using two software packages and the results were compared. For heptane annealed samples, the results were similar, and indicated that the sample had been patterned such that the nanostructures were non-interacting<sup>36</sup>. A sample of patterned CoPd alloy resulted in distinctly different FORC distributions, VARIFORC indicating a vortex switching mechanism with non-single domains., while FORC+ indicates non-interacting nanostructures<sup>36</sup>, correlated with SEM micrographs. Similar results were obtained for Co/Pd ML with a 100 nm Cr hard mask, though in this case, SEM micrographs

did not correlate any patterned nanostructures. FORC analysis could be a useful method to verify whether or not there exist nanostructures exist that may be difficult to image, or whether or not nanostructures on a patterned film are interacting, as well as the degree to which they are interacting.

## 7. OVERALL CONCLUSIONS

This dissertation discusses different methods to pattern a magnetic thin film with applications for magnetic storage media. The first chapter presented a brief overview of the history of magnetic storage media and discussed problems related to storage density, such as thermal stability and switching field distribution. Different methods of fabricating magnetic storage media, as well as their attendant difficulties were introduced. To achieve high areal density, a fabrication method must be able to produce magnetic media with small nanostructures that are thermally stable, writable and possess a sufficient signal-to-noise ratio.

The second chapter describes the equipment used to fabricate and measure our samples. The main deposition tools were the SFI Shamrock sputtering system, and a Denton e-beam evaporator. An Intevac ion mill with a Veeco ion source and SPTS RIE were used for etching and plasma ashing. Magnetic characteristic measurements were made using a Princeton Scientific alternating gradient magnetometer, and a JEOL 7000 FE-SEM was used to obtain images of the patterned films.

The third chapter described comparing two methods of phase separation annealing of a block copolymer. A matrix study of etch time and etch angle was undertaken for each phase separation method. It was found that ion milling at 45° and 3.5 minutes for the heptane annealing method yielded the highest coercivity. The average diameter of the heptane annealed samples was found to be ~33 nm, yielding an areal density<sup>11</sup> of ~300 Gb/in<sup>2</sup>, and the average diameter of the

air annealed nanopillars to ~22 nm, yielding an areal density<sup>11</sup> of ~ 400 Gb/in<sup>2</sup>. It seems the heptane annealing resulted in larger initial nanospheres compared to the air annealing process. It may be the result of the difference in solubility between heptane and toluene for PFS.

The fourth chapter described two different, but related experiments. The first part described using a different, smaller block copolymer as a template for magnetic media. The second part described using different thicknesses of Cr as a method to create a hard mask in conjunction with a block copolymer. The P2VP-b-PDMS produced nanospheres that are ~ 15 nm in diameter. However, the P2VP-b-PDMS did not survive the etching process. We coated magnetic thin films with P2VP-b-PDMS block copolymer, and then evaporation deposited 100, 30 and 20 nm of Cr on top of the samples. Evaporation generally has poor step coverage, and it was believed that using a CF<sub>4</sub> plasma would remove the PDMS nanospheres, lifting off the Cr, leaving behind a hard mask. The samples were etched in an ion mill with a variety of etch angles and times. The magnetic characteristics and SEM images suggest that the plasma ashing to lift off the Cr was not successful. A possible reason would be the thickness of the deposited Cr was too great, and therefore the plasma did not remove the PDMS nanospheres. A possible solution might be trying a thinner Cr layer or a different block copolymer.

Chapter five describes a method to create smaller nanospheres with block copolymers using a combination of ultrasound and a toluene bath. The ultrasonic process resulted in PFS nanospheres ~10 nm in diameter, with an areal density<sup>8</sup> of ~1250 Gb/in<sup>2</sup>. After etching, the patterned film yielded an areal density<sup>8</sup> of ~ 400 Gb/in<sup>2</sup>, however the pattern is difficult to see. A possible solution may be to attempt to improve the survivability of the PFS nanospheres, perhaps by coating the nanospheres with a metal, such as Cr.

The sixth chapter describes a potent analytical method, FORC analysis, to study the switching behavior of magnetic thin films. Two different software packages, VARIFORC and FORC+, were used and results compared. In particular, select samples from previous experiments were studied using this method. First, a heptane annealed sample was studied and the results from the two software packages were similar, and it was determined that the magnetic film was patterned into mainly non-interacting nanostructures. Next, a patterned CoPd alloy sample was analyzed, and the results of the two software packages were not the same. Since VARIFORC smooths the data more than FORC+, FORC+ may be more accurate. Magnetic film samples with a 100 nm Cr deposition and then etched were also studied, with similar results as above.

In conclusion, we have discussed a number of methods to pattern magnetic media. First, we optimized etch parameters for size and magnetic characteristics using a block copolymer pattern mask. Then we compared methods of phase separation for a block copolymer pattern mask to improve magnetic characteristics and size tuning. Then we attempted using a different block copolymer to improve size tuning, as well as using the block copolymer to fabricate a Cr hard mask. Next, a method to size tune a block copolymer using ultrasound and toluene is described. Finally, a powerful analytical method to study switching behavior was described. Table 7.1 below summarizes the as-deposited samples we investigated during this project.

Ta5/Pd5/[Co0.3/Pd1.0] <sub>14-20</sub> /Ta5 nm <sup>67</sup>
Ta5/Pd5/[Co0.3/Pd1.0] <sub>8</sub> /Ta5 nm
Ta5/Pd5/[Co <sub>25</sub> Pd <sub>75</sub> ]/Ta5 nm

Table 7.1 Magnetic Thin Films Investigated.

## REFERENCES

1. T. Hirano, P.-O. Jubert, D. Kerchner, J. Lille, Z. Liu, C. M. Mate, Y. Obukhov, K. C. Patel, K. Rubin, R. Ruiz, M. Schabes, L. Wan, D. Weller, T.-W. Wu, and E. Yang, "Bit Patterned Magnetic Recording: Theory, Media Fabrication, and Recording Performance", *IEEE Trans. Magn.* **51** (2015).
2. D. Thompson, J. S. Best, "The future of magnetic data storage technology", *IBM J. Res. Dev.*, **44**, 311 (2000).
3. M. H. Kryder, E. C. Gage, T. W. McDaniel, W. Challener, R. E. Rottmayer, G. Ju, Y.-T. Hsia, and M. F. Erden, "Heat Assisted Magnetic Recording", *Proc. IEEE*, **96**, 1810 (2008).
4. J.-G. Zhu, X. Zhu, and Y. Tang, "Microwave Assisted Magnetic Recording", *IEEE Trans. Magn.*, **44**, 125 (2008).
5. S. Y. Chou, M. S. Wei, P. R. Krauss, and P. B. Fischer, "Single-domain magnetic pillar array of 35 nm diameter and 65 Gbits/in<sup>2</sup> density for ultrahigh density quantum magnetic storage", *J. Appl. Phys.*, **76**, 6673 (1994).
6. R. M. H. New, R. F. W. Pease, and R. L. White, "Submicron patterning of thin cobalt films for magnetic storage", *J. Vac. Sci. Technol. B*, **12**, 3169 (1994).
7. T. R. Albrecht, O. Hellwig, R. Ruiz, M. E. Schabes, B. D. Terris, and X. Z. Wu, "Bit-Patterned Magnetic Recording: Nanoscale Magnetic Islands for Data Storage", in *Nanoscale Magnetic Materials and Applications*, J. P. Liu, E. Fullerton, O. Gutfleisch, and D. J. Sellmeyer, Eds. Springer US, 2009, pp. 237-274.
8. H.-J. Richter, A. Y. Dobin, O. Heinonen, K. Z. Gao, R. J. M. v. d. Veerdonk, R. T. Lynch, J. Xue, D. Weller, P. Asselin, M. F. Erden, and R. M. Brockie, "Recording on Bit-Patterned Media at Densities of 1 Tb/in<sup>2</sup> and Beyond", *IEEE Trans. Magn.*, **42**, 2255 (2006).
9. M. E. Schabes, "Micromagnetic simulations for terabit/in<sup>2</sup> head/media systems", *J. Magn. Magn. Mater.*, **320**, 2880 (2008).
10. S. J. Greaves, Y. Kanai, and H. Muraoka, "Magnetic Recording in Patterned Media at 5-10 Tb/in<sup>2</sup>", *IEEE Trans. Magn.*, **44**, 3430 (2008).
11. Y. Dong and R. H. Victora, "Micromagnetic Specification for Bit Patterned Recording at 4 Tb/in<sup>2</sup>", *IEEE Trans. Magn.*, **47**, 2652(2011).

12. E. C. Stoner, E. P. Wohlfarth, “A mechanism of magnetic hysteresis in heterogeneous alloys”, *Trans. R. Soc. A*, **240**, 599 (1948).
13. D. Suess, T. Schrefl, S. Fähler, M. Kirschner, G. Hrkac, F. Dorfbauer, and J. Fidler, “Exchange spring media for perpendicular recording”, *Appl. Phys. Lett.*, **87**, 012504, (2005).
14. P. Krone, D. Makarov, T. Schrefl, and M. Albrecht, “Exchange coupled composite bit patterned media”, *Appl. Phys. Lett.*, **97**, 082501 (2010).
15. L. Néel, “Théorie du trainage des ferromagnétiques en grains fins avec applications aux terres cuites”, *Ann. Géophys.* **5**, 99 (1949).
16. R. C. O’Handley, “Modern Magnetic Materials: Principles and Applications”, Wiley Inter-Science, 2000.
17. J. Kim, H. Zhao, Y. Jiang, A. Klemm, J. P. Wang, C. H. Kim, “Scaling analysis of In-Plane and Perpendicular Anisotropy Magnetic Tunnel Junctions Using a Physics-Based Model”, Device Research Conference (DRC), 72<sup>nd</sup> Annual (2014) Santa Barbara, CA USA.
18. O. Hellwig, A. Berger, T. Thomson, E. Dobisz, Z. Z. Bandic, H. Yang, D. S. Kercher, E. Fullerton, “Separating dipolar broadening from the intrinsic switching field distribution in perpendicular patterned media”, *Appl. Phys. Lett.*, **90**, 162516 (2007).
19. J. M Shaw, W. H. Rippard, S. E. Russek, T. Reith, C. M. Falco, “Origins of field switching distributions in perpendicular magnetic nanodot arrays”, *J. Appl. Phys.*, **101**, 023909 (2007).
20. I. Tagawa, Y. Nakamura, “Relationships between high density recording performance and particle coercivity distribution”, *IEEE Trans. Magn.*, **27** 4675 (1991).
21. J. Lee, C. Brombacher, J. Fidler, B. Dymerska, D. Suess, M. Albrecht, “Contribution of the easy axis orientation, anisotropy distribution and dot size on the switching field distribution of bit patterned media”, *Appl. Phys. Lett.*, **99**, 062505 (2011).
22. B. Pfau, C. M. Günther, E. Guehrs, T. Hauet, H. Yang, L. Vinh, X. Xu, D. Yaney, R. Rick, S. Eisebitt, O. Hellwig, “Origin of magnetic switching field distribution in bit patterned media based on pre-patterned substrates”, *Appl. Phys. Lett.*, **99**, 062502 (2011).
23. R. Dittrich, T. Schrefl, A. Thiaville, J. Miltat, V. Tsiantos, and J. Fidler, “Comparisons of Langevin dynamics and direct energy barrier computation”, *J. Magn. Magn. Mater.* **272** 276, 747(2004).
24. J. W. Lau, J. K. Bording, M. Beleggia, and Y. Zhu, “Energy barrier to magnetic vortex nucleation”, *Appl. Phys. Lett.* **88**, 012508 (2006).

25. J. Gadbois and J. G. Zhu, "Effect of edge roughness in Nano Scale Magnetic Bar Switching", *IEEE Trans. Magn.* 31, 3802 (1995).
26. J. W. Lau, R. McMichael, M. A. Schofield, and Y. Zhu, "Correlation of edge roughness to nucleation field distribution in patterned Permalloy elements", *J. Appl. Phys.*, 102, 023916 (2007).
27. M. Yoshigawa, E. Kitagawa, S. Takahashi, T. Kai, M. Amano, N. Shimonura, T. Kishi, S. Ikegawa, Y. Asao, H. Yoda, "Reduction of switching field distribution by edge oxidation of submicron magnetoresistive tunneling junction cells for high density magnetoresistive random access memories", *J. Appl. Phys.* 99, 08R 702 (2006).
28. G. Roy, D. E. Laughlin, T. J. Klemmer, K. Howard, S. Khizroev, D. Litinov, "Seed layer effect on the microstructure and magnetic properties of Co/Pd multilayers", *J. Appl. Phys.* 89, 7531 (2001).
29. K. J. Kirk, J. N. Chapman, S. McVitie, P. R. Atchison, C. D. Wilkinson, "Interactions and switching field distributions of nanoscale magnetic elements", *J. Appl. Phys.* 87, 5105 (2000).
30. J. W. Lau, R. D. McMichael, S. H. Chung, J. O Rantschler, V. Parekh, D. Litinov, "Microstructural origin of switching field distribution in patterned Co/Pd multilayer nanodots", *Appl. Phys. Lett.*, **92** 012506 (2008).
31. B. Pfau, C. M. Günther, E. Guehrs, T. Hauet, T. Hennen, S. Eisebitt, O. Hellwig, "Influence of stray fields on the switching-field distribution for bit patterned media based on pre-patterned substrates", *Appl. Phys. Lett.*, **105** 132407 (2014).
32. A. R. Muxworthy, A. P. Roberts, "First-order reversal curve (FORC) diagrams", *Encyclopedia of Geomagnetism and paleomagnetism*, Springer, 266 (2007).
33. C. R. Pike, A. P. Roberts, K. L. Verosub, "First-order reversal curve diagrams and thermal relaxation effects in magnetic particles" *Geophys J. Int.* 145, 721 (2001).
34. A. P. Roberts "First-order reversal curve diagrams: A new tool for characterizing the magnetic properties of natural samples" *J. Geophys. Res.* 105, 28461 (2000).
35. P. B. Visscher "FORC+: A method for separating reversible from irreversible behavior using first order reversal curves" arXiv:1610.09199 [cond-mat].
36. R. K. Dumas, C.-P. Li, I. V. Roshchin, I. K. Schuler, and K. Liu, "Magnetic fingerprints of sub-100 Fe dots", *Phys. Rev. B* **75** 134405 (2007).
37. F. S. Bates, G. H. Fredrickson, "Block Copolymer Thermodynamics: Theory and Experiment", *Annu. Rev. Phys. Chem.*, **41**, 525 (1990).

38. C. T. Black, R. Ruiz, E. M. Sikorski I. V. Babich, R. L. Sandstrom, K. W. Guarini, Y. Zhang, “Polymer self-assembly in semiconductor microelectronics”, IBM J. Res. Dev. **51**, 605 (2007).
39. J. W. Jeong, W. I. Park, M. J. Kim, C. A. Ross, and Y. S. Jung, “Highly Tunable Self-Assembled Nanostructures from a Poly(2-vinylpyridine-b-dimethylsiloxane) Block Copolymer”, *Nano. Lett.*, 2011, *11*(10), pp 4095-4101.
40. S. Y. Chou, P. R. Krauss, P. J. Renstrom, “Imprint Lithography with 25-Nanometer Resolution”, *Science*, **272**, 85 (1996).
41. D. J. Resnick, W. J. Dauksher, D. Mancini, K. J. Nordquist, T. C. Bailey, S. Johnson, N. Stacey, J. G. Ekerdt, C. G. Willson, S. V. Sreenivasan, N. Schumaker, “Imprint lithography for integrated circuit fabrication”, *J. Vac. Sci. Technol. B*, **21**, 2624 (2003).
42. E. A. Costner, M. W. Lin, W.-L. Jen, C. G. Willson, “Nanoimprint Lithography Materials Development for Semiconductor Device Fabrication”, *Annu. Rev. Mater. Res.*, **39**, 155 (2009).
43. S. Y. Chou, P. R. Krauss, L. Kong, “Nanolithographically defined magnetic structures and quantum magnetic disk (invited)”, *J. Appl. Phys.*, **79**, 6101 (1996).
44. Natajarathinam, Anusha (2012). *Exploration of Perpendicular Magnetic Anisotropy Material System for Application in Spin Transfer Torque-Random Access Memory (STT-RAM)* Doctoral dissertation. University of Alabama.
45. Su, Hao (2014). *Nanostructured Magnetic Recording Media by Patterning and Glancing Angle Deposition* Doctoral dissertation. University of Alabama.
46. P. J. Flanders, “An alternating gradient magnetometer”, *Journal of Applied Physics*, Vol 63, 3940 (1988).
47. The University of Alabama Central Analytical Facility, retrieved October 28, 2017, from <https://caf.ua.edu/>
48. T. Thomson, G. Hu, and B. D. Terris, “Intrinsic Distribution of Magnetic Anisotropy in Thin Films Probed by Patterned Nanostructures”, *Phys. Rev. Lett.* **96**, 257204 (2006).
49. D. Goll and T. Bublath, “Large-area hard magnetic L1<sub>0</sub>-FePt and composite L1<sub>0</sub>-FePt based nanopatterned”, *Phys. Status Solidi A* **210**, 1261 (2013).
50. M. H. Kryder, E. C. Gage, T. W. McDaniel, W. A. Challener, R. E. Rottmayer, G. Ju, Y.-T. Hsia, and M. F. Erden, “Heat Assisted Magnetic Recording”, *Proc. IEEE* **96**, 1810 (2008).

51. D. E. Laughlin, K. Srinivasan, M. Tanase, L. Wang, “: Crystallographic aspects of L1<sub>0</sub> magnetic material”, *Scr. Mater.* **53**, 383 (2005).
52. O. Hellwig, T. Hauet, T. Thomson, E. Dobisz, J. D. Risner-Jamtgaard, D. Yaney, B. D. Terris, and E. E. Fullerton, “Coercivity tuning in Co/Pd multilayer systems based bit patterned media”, *Appl. Phys. Lett.* **95**, 232505 (2009).
53. O. Hellwig, J. K. Bosworth, E. Dobisz, D. Kercher, T. Hauet, G. Zeltzer, J. D. Risner-Jamtgaard, D. Yaney, and R. Ruiz, “Bit patterned media based on block copolymer directed assembly with narrow magnetic switching field distribution”, *Appl. Phys. Lett.* **96**, 052511 (2010).
54. T. Bublat and D. Goll, “Large-area hard magnetic L1<sub>0</sub>-FePt nanopatterned by nanoimprint lithography”, *Nanotechnology* **22**, 315301 (2011).
55. R. A. Griffiths, A. Williams, C. Oakland, J. Roberts, A. Vijayaraghavan, and T. Thomson, J., “Directed self-assembly of block copolymers for use in bit patterned media fabrication”, *Phys. D: Appl. Phys.* **46**, 503001 (2013).
56. H. Su, S. C. Schwarm, R. L. Martens, and S. Gupta, “Microstructure evolution and magnetic properties of FeB/Pt multilayers and FeBPt composite films”, *J. Appl. Phys.*, **115**, 17B717 (2014).
57. Z. Sun, D. Li, A. Natarajarathinam, H. Su, and S. Gupta, “Large area patterning of single magnetic domains with assistance of ion irradiation in ion milling”, *J. Vac. Sci. Technol. B* **30**, 031803 (2012).
58. H. Su, A. Natarajarathinam, and S. Gupta, “Nanorods of Co/Pd multilayers fabricated by glancing angle deposition for advanced media”, *J. Appl. Phys.* **113**, 203901 (2013).
59. J. Abugri, P. B. Visscher, H. Su, and S. Gupta, “Modeling interface exchange coupling: Effect on switching of granular FePt films”, *J. Appl. Phys.*, **118**, 043902(2015).
60. H. Su, S.C. Schwarm, R. Douglas, A. Montgomery, A.G. Owen and S. Gupta, “(111) Orientation preferred L1<sub>0</sub> FeBPt patterned by block copolymer templating”, *J. Appl. Phys.* **116**, 113906 (2014).
61. J. Y. Cheng, C. T. Rettner, D. P. Sanders, H. C. Kim, and W. D. Hinsberg, “Dense Self-Assembly on Sparse Chemical Patterns: Rectifying and Multiplying Lithographic Patterns Using Block Copolymers”, *Adv. Mater.* **20**, 3155 (2008).
62. J. G. Son, J.-B. Chang, K. K. Berggren, and C. A. Ross, “Assembly of Sub-10-nm Block Copolymer Patterns with Mixed Morphology and Period Using Electron Irradiation and Solvent annealing”, *Nano. Lett.* **11**, 5079 (2011).

63. C. Tang, E. M. Lennon, G. H. Fredrickson, E.d J. Kramer, Craig J. Hawker, “Evolution of Block Copolymer Lithography to Highly Ordered Square arrays”, *Science*, **322**, 429 (2008).
64. J. N. L. Albert and Thomas H. Epps, III, “Self-assembly of block copolymer thin films”, *Materials Today*, **13**,24 (2010).
65. K. W. Gotrik and C. A. Ross, “Solvothermal Annealing of Block Copolymer Thin Films”, *Nano. Lett.*, **13**, 5117 (2013).
66. C. T. O’Mahony, D. Borah, and M. A. Morris, “Microphase Separation of a PS-b-PFS Block Copolymer via Solvent Annealing: Effect of Solvent, Substrate and Exposure Time on Morphology”, *Morris, Int. J. Poly. Sci.*, **2015**, 270891 (2015).
67. A. G. Owen, H. Su, A. Montgomery, R. Douglas, and S. Gupta, “Statistical Optimization of Co/Pd Multilayer Patterned via Block Copolymer Templating”, *TMS 2015 Supp. Proc.*, p.309 John Wiley and Sons (2015).
68. X. Li, Z. R. Tadisina, G. Ju, and S. Gupta, “Preparation and properties of perpendicular CoPt magnetic nanodot arrays patterned by nanosphere lithography”, *J. Vac. Sci. Technol., A* **27**, 1062 (2009).
69. J. Fassbender, D. Ravelsona, Y. Samson, “Tailoring magnetism by light-ion irradiation”, *J. Phys. D: Appl. Phys.* **37**, R179 (2004).
70. Z. Sun, S. T. Retterer, and D. Li, “The influence of ion-milling damage to magnetic properties of Co<sub>80</sub>Pt<sub>20</sub> patterned perpendicular media”, *J. Phys. D: J. Appl. Phys.*, **47** 105001 (2014).
71. T. Koda, H. Awano, H. Hieda, K. Naito, A. Kikitsu, T. Matsumoto, K. Nakamura, and T. Nishida, “Study of high magnetic anisotropy Co/Pd multilayers for patterned media”, *J. Appl. Phys.* **103**, (2008) 07C502.
72. J. K. Yang, Y. Chen, T. Huqang, H. Duan, N. Thiyagarajah, H. K. Hiu, S. Leong and V. Ng, “Fabrication and characterization of bit-patterned media beyond 1.5 Tb/in<sup>2</sup>”, *Nanotechnology* **22**, (2011) 385301.
73. J. Y. Cheng, F. Zhang, H. I. Smith, G. J. Vancso, and C. A. Ross, “Patter Registration Between Spherical Block-Copolymer Domains and Topographical Templates”, *Adv. Mater.* **18**, (2006) 597.
74. J. Wang, M. Pelletier, H. Zhang, H. Xia, and Y. Zhao, “High Frequency Ultrasound-Responsive Block Copolymer Micelle” *Langmuir* **2009** 25(22), 13201-13205.

75. R. Sbiaa and S. N. Piramanaygam, “Patterned Media Towards Nano-bit Magnetic Recording: Fabrication and Challenges”, *Recent Patents on Nanotechnology* 2007, *1*, 29-40.
76. R. Egli “VARIFORC: An optimized protocol for calculating non-regular first-order reversal curve (FORC) diagrams” *Glob. Planet. Chang.* 110, 302 (2013).